# Conjugation of Oligo-His Peptides to Magnetic $\gamma$-Fe 2 O 3 @SiO 2 Core–Shell Nanoparticles Promotes Their Access to the Cytosol

Mathilde Le Jeune, Emilie Secret, Michaël Trichet, Aude Michel, Delphine Ravault, Françoise Illien, Jean-Michel Siaugue, Sandrine Sagan, Fabienne Burlina, Christine Ménager

## To cite this version:

Mathilde Le Jeune, Emilie Secret, Michaël Trichet, Aude Michel, Delphine Ravault, et al.. Conjugation of Oligo-His Peptides to Magnetic $\gamma$-Fe 2 O 3 @SiO 2 Core–Shell Nanoparticles Promotes Their Access to the Cytosol. ACS Applied Materials & Interfaces, 2022, 14 (13), pp.15021-15034. 10.1021/acsami.2c01346 . hal-03810702v2

HAL Id: hal-03810702
https://hal.science/hal-03810702v2

Submitted on 11 Oct 2022

# Conjugation of oligo-His peptides to magnetic $\gamma$-$Fe_2O_3$@$SiO_2$ core-shell nanoparticles promotes their access to the cytosol

*Mathilde Le Jeune,*[a,b] *Emilie Secret,*[a] *Michaël Trichet,*[c] *Aude Michel,*[a] *Delphine Ravault,*[b] *Françoise Illien,*[b] *Jean-Michel Siaugue,*[a] *Sandrine Sagan,*[b] *Fabienne Burlina,**[b] *Christine Ménager**[a]

[a] Sorbonne Université, CNRS, Laboratoire Physicochimie des Électrolytes et Nanosystèmes Interfaciaux, PHENIX, 75005 Paris, France.

[b] Sorbonne Université, École normale supérieure, PSL University, CNRS, Laboratoire des Biomolécules, LBM, 75005 Paris, France.

[c] Sorbonne Université, CNRS, Institut de Biologie Paris-Seine (IBPS), Service de microscopie électronique (IBPS-SME), 9 quai Saint Bernard, F-75005, Paris, France

**KEYWORDS:** cationic peptides, cell-penetrating peptides, magnetic core-shell nanoparticles, click chemistry, endosomal escape

## ABSTRACT:

The endosomal entrapment of functional nanoparticles is a severe limitation to their use for biomedical applications. In the case of magnetic nanoparticles (MNPs), this entrapment leads to poor heating efficiency for magnetic hyperthermia and suppresses the possibility to manipulate them in the cytosol. Current strategies to limit their entrapment include functionalization with cell-penetrating peptides to promote translocation directly across the cell membrane or facilitate endosomal escape. However, these strategies suffer from potential release of free peptides in the cell and to the best of our knowledge there is currently a lack of effective methods for the cytosolic delivery of MNPs after incubation with cells.

Herein, we report the conjugation of fluorescently labelled cationic peptides to $\gamma$-$Fe_2O_3$@$SiO_2$ core-shell nanoparticles by click chemistry to improve MNP access to the cytosol. We compare the effect of $Arg_9$ and $His_4$ peptides. On one hand, $Arg_9$ is a classical cell-penetrating peptide, able to enter cells by direct translocation and on the other hand, it has been demonstrated that sequences rich in histidine residues can promote endosomal escape, possibly by the proton sponge effect. The methodology developed here allows a high co-localization of the peptides and core-shell nanoparticles in cells and confirms that grafting peptides rich in histidine residues onto nanoparticles promotes NPs access to the cytosol. Endosomal escape was confirmed by a calcein leakage assay and by ultrastructural analysis in transmission electron microscopy. No toxicity was observed for the peptide-nanoparticles conjugates. We also show that our conjugation strategy is compatible with the addition of multiple substrates and can thus be used for the delivery of cytoplasm-targeted therapeutics.

## 1. INTRODUCTION

Magnetic nanoparticles (MNPs) have emerged as an important class of functional nanomaterials in the biomedical field for various applications such as magnetic hyperthermia to kill cancer cells, magnetic resonance imaging, drug delivery, or cellular engineering.[1,2] For some of these applications, MNP entry inside cells is required. However, similar to most other types of nanoparticles, MNPs enter cells by endocytosis and often remain trapped inside endosomes. Confinement of MNPs in these small intracellular vesicles, restricts the ease of magnetic manipulation[3,4] and also prevents the MNPs from interacting with targets present in the cytosol or other organelles. Moreover the aggregation of the MNPs inside the endosomes has been shown to negatively impact their heating efficiency in magnetic hyperthermia due to dipolar interactions between the MNPs, limiting the development of magnetic hyperthermia-based treatment of cancer.[3] In cellular engineering, MNPs have recently been used to remotely control cellular functions, often referred to as "magnetogenetics".[5–7] This approach is primarily used for the control of extracellular proteins or ion channels due to the difficulties in avoiding endosomal confinement of MNPs after their cellular uptake. Easy access to intracellular proteins capable of triggering a cascade of signaling events would greatly expand the potential of magnetic nanoparticles for cellular engineering. For example, the GTPases Ras, Rac or Cdc42 are intracellular proteins which are involved in signaling pathways in neurons, and are targets of choice for magnetic cellular manipulation to induce neuronal growth. Their activation with functionalized MNPs has been achieved, albeit with particles that were directly micro-injected in cells.[5,6,8] Unfortunately, micro-injections can only be performed on a small number of cells, making the process difficult to parallelize. Finding a way to overcome the endosomal entrapment of MNPs to enable their diffusion into the cytosol would be a key step for the development of applications such as magnetic hyperthermia for cancer treatment and remote control of cellular processes.

In recent years, cell penetrating peptides (CPPs), which often correspond to relatively short cationic or amphipathic sequences, have shown promise in mediating the transport of a wide range of modalities such as peptides, proteins and oligonucleotides.[9,10] Cellular uptake of CPPs mostly occurs by endocytosis. However, some CPPs can also enter cells by direct translocation, a process which involves a transient perturbation of the lipid bilayer of the plasma membrane and allows the CPP and its cargo to directly reach the cytosol.[11–15] The conjugation of CPPs onto the surface of nanoparticles has been previously reported.[16] For example, the TAT peptide has been grafted onto CdSe-ZnS quantum dots[17] and poly-arginine CPPs (or lipidated derivatives) onto superparamagnetic iron oxide nanoparticles (SPION) and gold nanoparticles.[18,19] In all cases the CPPs were found to improve nanoparticle (NP) cellular uptake, although the endocytic pathways remained dominant and NPs were not visualized in the cytosol. Interestingly, efficient siRNA nanocarriers have been engineered by combining NPs and CPPs, where the CPP was used both to load the siRNAs *via* electrostatic interactions as well as to improve siRNA cytosolic delivery. In particular, SPIONs derivatized with both poly-arginine and gH625 CPPs[20] and chitosan NPs functionalized with poly(histidine-arginine)$_6$ peptide[21] were shown to promote siRNA endosomal escape. Whilst the cellular distribution of the chitosan nanocarrier was not analyzed,[21] Ben Djemaa *et al.*, suggested in their study that the SPION nanocarriers remained trapped inside endosomes/lysosomes.[20]

The scope of this study was to improve access to the cytosol of the MNPs, which is essential for innovative cellular engineering applications. We have investigated the impact of MNP functionalization with two basic peptides, a poly-Arg peptide (Arg$_9$) and a short His-rich peptide (His$_4$-Trp), on the internalization process of MNPs. Arg$_9$ is a classical CPP, which has been shown to enter cells by both endocytosis and direct translocation.[22–24] The capability of Arg$_9$ to transiently destabilize the plasma membrane or endosomal membranes to reach the cytosol is however strongly dependent on different parameters including its concentration and the nature and size of the transported cargo.[13,16,22–24] On the other hand, oligo-His sequences have been shown to promote endosomal escape, possibly by the so-called "proton sponge effect". It has been proposed that protonation of the imidazole group of His residues, which can occur in the acidic lumen of late endosomes, can induce proton and chloride ion accumulation resulting in osmotic swelling and subsequent rupture of endosomes.[25–27] It has also recently been shown that conjugation of a short oligo-His peptide could induce endosomal escape using calcein-loaded mesoporous silica NPs.[28]

The MNPs selected in this study were core-shell $\gamma$-$Fe_2O_3$@$SiO_2$ nanoparticles. These core-shell $\gamma$-$Fe_2O_3$@$SiO_2$ nanoparticles were chosen for several reasons. They can be synthesized with sizes suitable for biomedical applications and maintain good colloidal stability after functionalization. They can also easily be rendered fluorescent by the addition of a fluorophore in the silica shell, which enables their visualization through fluorescence and confocal microscopy. Finally, a wide range of functionalization strategies are available due to well established silica chemistry.

A covalent grafting of the peptides onto core-shell nanoparticles was favored in this study over a non-covalent approach to facilitate the nanoparticle-peptide conjugate tracking in complex biological environments. The covalent bond also prevents uncontrolled peptide release in biological media.

Among the different chemoselective ligation methodologies, copper-free click chemistry is widely studied for its ease of implementation, high yield and non-cytotoxicity.[29] The methodology involves the cycloaddition reaction between a constrained alkyne (e.g. dibenzocyclooctyne (DBCO)), and an azide. In this work the $\gamma$-$Fe_2O_3$@$SiO_2$ nanoparticles were functionalized with a DBCO group, while the peptides were designed to carry the azido group. We report here an optimized protocol that allows the efficient covalent grafting of peptides onto core-shell nanoparticles. We also demonstrate the possibility to graft two different substrates at the surface of MNPs. After incubation with the cells, the polyhistidine-functionalized nanoparticles showed partially diffused cytosolic fluorescence by confocal microscopy, suggestive of enhanced endosomal escape. In contrast, non-functionalized and polyarginine-functionalized MNPs exhibited exclusively a punctuate fluorescent signal. The capability of the polyhistidine-functionalized nanoparticles to perturb the membrane of endosomes was further confirmed by a calcein leakage assay. Importantly, endosomal membrane ruptures were observed and free MNPs were detected in the cytosol by ultrastructural analysis in transmission electron microscopy.

## 2. EXPERIMENTAL SECTION

### 2.1 Materials

Standard Fmoc amino acids, were purchased from Iris Biotech (Germany). Rink Amide AM resin, *N,N'*-Diisopropylcarbodiimide (DIC), 1-Hydroxybenzotriazole hydrate (HOBt), *N,N,N',N'*-Tetramethyl-*O*-(1*H*-benzotriazol-1-yl)uronium hexafluorophosphate (HBTU), *N,N*-Diisopropylethylamine (DIEA), ethylenediaminetetraacetic acid (EDTA) $Pd(PPh_3)_4$, $PhSiH_3$, Fmoc-ε-Ahx-OH and $N_3$-$CH_2$-COOH, Tetraethylorthosilicate (TEOS), citric acid, 3-aminopropyltriethoxysilane (APTS), rhodamine B isothiocynate, Dimethylsulfoxyde (DMSO), dibenzocyclooctyne-$PEG_4$-N-hydroxysuccinimidyl ester, tri-sodium citrate dihydrate, 3-morpholinopropane-1-sulfonic acid (MOPS) buffer, 4-(2-hydroxyethyl)-1-piperazineethanesulfonic acid buffer (HEPES), Hanks balanced salt solution (HBSS), fetal bovine serum (FBS), Hoechst 33342 dye, calcein, trypan blue 0.4%, glutaraldehyde, fluorescamine and Epon resin were purchased from Sigma-Aldrich (France). Dimethylformamide (DMF) (Peptide synthesis grade), acetonitrile (HPLC grade), trifluoroacetic acid (TFA) (Optical spectroscopy grade), dichloromethane (Analysis grade), piperidine (Peptide synthesis grade) and citric acid were obtained from Carlo Erba (France). Ferrous chloride, ferric chloride, ferric nitrate, acetone, diethyl ether, ethanol (96%), nitric acid (68%), hydrochloric acid 37% and ammonia (20%) were provided by VWR (France). 2-(methoxy(polyethyleneoxy)propyl)trimethoxysilane (PEOS) was obtained from ABCR (Germany). Dulbecco's modified Eagle's-F12 medium (DMEM-F12), penicillin, streptomycin, amphotericin B and trypsin were purchased from Gibco (France). Lactacte dehydrogenase (LDH) was provided by Invitrogen (France). Wild type Chinese Hamster Ovary (CHO-K1) cells (reference CCL-61) were obtained from ATCC (USA).

## 2.2 Peptide synthesis

### *2.2.1 Fluorescent azidopeptide derivatives CF-R9 and CF-H4*

The fluorescent peptides **CF-R9** (CF-Ahx-Lys(CO-$CH_2$-$N_3$)-$(Arg)_9$-$NH_2$, CF: 5(6)-carboxyfluorescein) and **CF-H4** (CF-Ahx-Lys(CO-$CH_2$-$N_3$)-$(His)_4$-Trp-$NH_2$) were obtained by Fmoc solid-phase peptide synthesis (SPPS). The $Arg_9$ sequence was assembled on Rink amide Protide LL (CEM Corporation) by automated microwave-assisted SPPS using a Liberty Blue synthesizer (CEM Corporation) at the "Plateforme d'ingénierie des protéines" (IBPS, Sorbonne Université). It was then elongated manually to give **CF-R9**. The **CF-H4** peptide was synthesized manually in a polypropylene vessel on Rink Amide AM resin (0.35 mmol/g resin, 0.1 mmol scale). For the manual elongations of both peptides, Fmoc protected amino acids and Ahx linker (5 equiv.) were activated for 3 min with HBTU (4.5 equiv.) and DIEA (10 equiv.) in DMF before addition to the peptide-resin. The coupling reactions were then allowed to proceed for 30 min at room temperature (RT). Fmoc deprotections were performed using a 20% v/v solution of piperidine in DMF (3 + 7 min). 5(6)-carboxyfluorescein (5 equiv.) was coupled on the *N*-terminus of the peptide using DIC (5 equiv.) and HOBt (10 equiv.) in DMF (15 min activation, 15 h coupling at RT). The resin was then washed several times with a 20% v/v solution of piperidine in DMF. Selective Alloc removal from the Lys side chain was then performed by treatment of the peptide-resin with a solution of $Pd(PPh_3)_4$ (0.25 equiv.), $PhSiH_3$ (25 equiv.) in dichloromethane for 90 min at RT under argon, then the resin was washed using a 20% v/v solution of piperidine in DMF. This was followed by coupling of $N_3$-$CH_2$-COOH (5 equiv.) on the Lys side chain using DIC (5 equiv.) and HOBt (10 equiv.) in DMF (15 min activation, 15 h coupling at RT). Final peptide deprotection and cleavage from the resin was achieved by treatment with a solution containing 95% TFA, 2.5% $H_2O$ and 2.5% triisopropylsilane for 4 h at RT. The peptides were precipitated with cold diethyl ether and incubated for at least 30 min at -20 °C, and pelleted by centrifugation. Peptides were purified by reverse phase HPLC (RP-C18 column, 5 $\mu$m, 250 x 16 mm, Macherey Nagel) using a flow rate of 10 mL/min and a linear gradient over 30 min of 10-40% of solvent B in A for **CF-R9** and 1-30% B in A for **CF-H4** (A: 0.1% TFA in $H_2O$, B: 0.1% TFA in $CH_3CN$). Peptides were monitored at 220 nm. The purity of the fractions was assessed by HPLC (RP-C18 column, 5 $\mu$m, 100 x 4.6 mm, Higgins Analytical) at a flow rate of 1 mL/min with a linear gradient of solvent B in A over 10 min (Figure S1). Peptides were monitored at 220 nm. Fractions containing the pure desired peptide were combined and lyophilized.

The peptides were characterized by Matrix Assisted Laser Desorption Ionization - Time of Flight (MALDI-TOF) mass spectrometry (Applied Biosystems 4700 or AB Sciex Voyager DE-PRO spectrometer) in positive ion mode, reflector, using CHCA (α-cyano-4-hydroxycinnamic acid) at 10 mg/mL in $H_2O/CH_3CN$/TFA (1/1/0.01) as matrix. **CF-R9**, expected m/z $[M+H]^+$: 2106.19, observed m/z $[M+H]^+$: 2106.41. **CF-H4**, expected m/z $[M+H]^+$: 1435.59, observed m/z $[M+H]^+$: 1435.92. In both cases, an additional peak was observed (Δ m/z: -28), suggesting a fragmentation of the azido group *via* expulsion of $N_2$ during MALDI-TOF analysis, as previously reported.[30]

### *2.2.2 Azidopeptide derivatives R9* and H4**

Peptides **R9*** ($N_3$-$CH_2$-CO-(Arg)$_9$-$NH_2$) and **H4*** ($N_3$-$CH_2$-CO-(His)$_4$-Trp-$NH_2$) were synthesized as described above by Fmoc solid-phase chemistry. $N_3$-$CH_2$-COOH was in this case introduced on the peptide *N*-terminus. Peptides were purified by reverse phase HPLC (RP-C18 column, 5 $\mu$m, 250 x 16 mm, Macherey Nagel) using a flow rate of 10 mL/min and a linear gradient over 30 min of 0-40% solvent B in A for **R9*** and 1-30% of solvent B in A for **H4***. The purity of the fractions was checked by analytical HPLC (Figure S1). The peptides were characterized by MALDI-TOF MS as described above (Figure S2). **R9***, m/z $[M+H]^+$: 1505.95 (expected), 1505.79 (observed). **H4***, m/z $[M+H]^+$:835.36 (expected), 835.28 (observed). In both cases, an additional peak was observed (Δ m/z: -28), suggesting a fragmentation of the azido group *via* expulsion of $N_2$ during MALDI-TOF analysis, as previously reported.[30]

## 2.3 Nanoparticles synthesis

### *2.3.1 Maghemite nanoparticles $\gamma$-$Fe_2O_3$*

The size sorted maghemite nanoparticles were obtained by alkaline co-precipitation.[31] A solution of ammonia 22.5% in $H_2O$ (1 L) was added to an acidic iron (II) and iron (III) ions solution (180 g of $FeCl_2$, 100 mL of HCl 37%, 500 mL of deionized (DI) $H_2O$, 715 mL of $FeCl_3$ 27%) and left at room temperature under stirring for 30 min. After rinsing with DI $H_2O$, the obtained $Fe_3O_4$ nanoparticles were redispersed in 360 mL of nitric acid (52%), the solution was agitated for 10 min, and the particles were magnetically separated from the solution. A solution of iron (III) nitrate (323 g) in DI $H_2O$ (800 mL) was then added, and the combined mixture was boiled (150 °C) for 30 min to give $\gamma$-$Fe_2O_3$ nanoparticles.

The resulting nanoparticles were acidified with nitric acid (52%, 360 mL) and washed with acetone (3x, 1 L) and diethyl ether (2x, 0.5 L) before they were redispersed in DI $H_2O$ (1 L), resulting in $\gamma$-$Fe_2O_3$ nanoparticles which are polydisperse in size. To decrease the polydispersity, a size sorting process was performed.[32] The addition of nitric acid (52.5%, 30 mL) increased the ionic strength, leading to the flocculation of the larger, less stable, nanoparticles. These precipitated nanoparticles were separated from the rest of the magnetic fluid, washed with acetone (0.5 L) and diethyl ether (0.3 L), and finally redispersed in DI $H_2O$. To ensure their stability and dispersion at neutral pH, the nanoparticles were citrated by heating the dispersion (150 °C) with sodium citrate (4.5 g, 0.125 M) for 30 min. After washing with acetone (0.5 L) and diethyl ether (0.3 L), the resulting nanoparticles were dispersed in DI $H_2O$ to give a final iron concentration of 1.07 M.

### *2.3.2 $\gamma$-$Fe_2O_3$@$SiO_2$ Core-Shell Nanoparticles CS*

Tetraethyl orthosilicate (112 µL, 0.50 mmol TEOS), 30% ammonia solution (250 µL, 3.9 mmol), and aminopropyltriethoxysilane functionalized rhodamine B (18.6 µL, 0.076 µmol APTS) were added to a solution of $\gamma$-$Fe_2O_3$ nanoparticles (125 µL, [Fe] = 0.13 mmol) in 1:2 DI $H_2O$/ethanol (15 mL). The mixture was agitated for 2 h at RT. The silica shell was functionalized by the addition of TEOS (39.1 µL, 0.18 mmol), trimethoxysilane 3-[methoxy(polyethyleneoxy) propyl] (PEOS) (40.7 µL, 0.075 mmol) and APTS (19.7 µL, 0.084 mmol). The mixture was stirred for 15 h at RT. The resulting nanoparticles were then rinsed with diethyl ether/ethanol 15:1 (3x, 30 mL) and redispersed in 5 mL of a 3-morpholinopropane-1-sulfonic acid (MOPS) buffer (0.1 M, pH = 7.4). The obtained core-shell nanoparticles were characterized by TEM. The iron concentration of **CS** was 24 mM. The suspension was stable at 4 °C for six months.

### *2.3.3 Dibenzocyclooctyne-Functionalized Core-Shell Nanoparticles DBCO-CS*

**DBCO(a)-CS** and **DBCO(b)-CS** were synthesized by adding 3.8 $\mu$L and 1.9 $\mu$L dibenzocyclooctyne-PEG$_4$-*N*-hydroxysuccinimidyl ester (10 mM in dimethylsulfoxyde (DMSO)) respectively to a solution of core-shell nanoparticles **CS** (100 µL, [Fe] = 24 mM) dispersion in MOPS (0.1 M, pH 7.4). The mixtures were incubated for 1 h at RT. The DBCO-functionalized nanoparticles were then applied onto Sephadex G-25 steric exclusion column (PD10 columns, GE Healthcare) and washed with HEPES buffer (0.2 M, pH = 7.4). The iron concentrations of **DBCO(a)-CS** and **DBCO(b)-CS** were 18 mM.

### 2.3.4 Carboxyfluorescein Peptide-Functionalized Core-Shell Nanoparticles CF-R9-CS

A solution of **CF-R9** peptide in $H_2O$ (19.0 µL, 1.00 mM) was incubated with a suspension of **DBCO(a)-CS** (100 µL, [Fe] = 18 mM) at a molar ratio 2:1 (DBCO:$N_3$-peptide) at RT for 15 h. **CF-R9-CS** nanoparticles were purified using Nanosep with a cut-off of 10 kDa eluting with EDTA 2 mM in HEPES buffer (0.2 M, pH 7.4). The iron concentration of **CF-R9-CS** was 13 mM. The suspensions were stable for one month.

### 2.3.5 Carboxyfluorescein Peptide-Functionalized Core-Shell Nanoparticles CF-H4-CS

A solution of **CF-H4** peptide in $H_2O$ (9.5 µL, 1.00 mM) was incubated with a suspension of **DBCO(b)-CS** (100 µL, [Fe] = 18 mM) at a molar ratio 2:1 (DBCO:$N_3$-peptide) at RT for 15 h. **CF-H4-CS** nanoparticles were purified using Nanosep with a cut-off of 10 kDa eluting with EDTA 2 mM in HEPES buffer (0.2 M, pH 7.4). The iron concentration of **CF-H4-CS** was 13 mM. The suspensions were stable for two weeks.

### 2.3.6 Bi-Functionalized Nanoparticles cy5/CF-R9-CS

A solution of peptide **CF-R9** (9.5 µL, 1.00 mM) in $H_2O$ was incubated with a suspension of **DBCO(a)-CS** (100 µL, [Fe] = 18 mM) at RT for 5 h, then a solution of cy5-$N_3$ (9.5 µL, 1.00 mM) in $H_2O$ was added to the suspension at RT and reacted for 15 h. **cy5/CF-R9-CS** was purified using Nanosep with a cut-off of 10 kDa eluting with EDTA 2 mM in HEPES buffer (0.2 M, pH 7.4). The iron concentration of **cy5/CF-R9-CS** was 11 mM.

## 2.4 Nanoparticle characterization techniques

### *2.4.1 Atomic Absorption Spectroscopy (AAS)*

The total iron concentration was determined by atomic absorption spectrophotometry at 248 nm (PerkinElmer Pinaacle 500). Before AAS measurements, nanoparticles were mineralized using concentrated hydrochloric acid (37%) and then diluted with nitric acid (2%).

### *2.4.2 Fluorescence spectroscopy*

The presence of rhodamine was investigated by fluorescence spectroscopy. The measurements were performed on a fluorescence spectrophotometer (Cary Eclipse). Fluorescence emission spectra were recorded in the range from 550 to 650 nm, using the excitation wavelength at 540 nm (Figure S5).

### *2.4.3 Transmission Electron Microscopy (TEM)*

The morphology and size of the nanoparticles were characterized using a JEOL-1011 transmission electron microscope. A droplet of diluted nanoparticle suspension in $H_2O$ was deposited on a carbon-coated copper grid, and the excess was drained using a filter paper. Size analysis was achieved in TEM images using ImageJ software.[33]

### *2.4.4 Magnetic measurement*

A suspension of $\gamma$-$Fe_2O_3$ nanoparticles was introduced in a sample capsule for vibrating sample magnetometry (VSM) analysis (Quantum Design, Versalab). Field-dependent magnetization curves were measured at 300 K as a function of the external field, in the range of $-7.10^5$ to $+7.10^5$ A/m to obtain saturation magnetization. The magnetic moment recorded (in A/m) can be converted to give the magnetization at saturation of the material expressed in emu/g of $\gamma$-$Fe_2O_3$.

### *2.4.5 Size and zeta potential analysis*

The hydrodynamic diameters and zeta potential of the samples were determined in $H_2O$ (viscosity of 0.8872 cP, refractive index (RI) of 1.330) at 25 °C. Dynamic Light Scattering (Nano ZS, Malvern, United Kingdom) was set up with detection angle at 173° and automatic optimization of conditions.

### *2.4.6 Fluorescamine assay*

APTS standard solutions, 0 $\mu$M, 2 $\mu$M, 8 $\mu$M, 14 $\mu$M, 20 $\mu$M and 26 $\mu$M were prepared in a solution of fluorescamine (0.2 M in EtOH). 20 $\mu$L of the nanoparticle suspensions were added in 5 mL of a fluorescamine solution (0.2 M in EtOH). The solutions were kept in the dark for 2 h. Fluorescence emissions were recorded at 480 nm, using an excitation wavelength of 390 nm. Based on the APTS calibration curve, the concentration of amine in each sample was determined.

### *2.4.7 Estimation of the number of peptide per core-shell nanoparticle*

The number of peptides (**CF-R9** or **CF-H4**) per core-shell NP was determined by using the fluorescence property of the carboxyfluorescein present in the **CF-R9** and **CF-H4** peptides. First, were prepared solutions of peptides **CF-R9** and **CF-H4** at different concentrations (from 0.16 $\mu$M to 1 $\mu$M) in HEPES buffer (0.2 M, pH 7.4). Then fluorescence intensity was measured at 525 nm by exciting the solutions at 505 nm. Next, a linear calibration curve was obtained by plotting the fluorescence intensity against **CF-R9** and **CF-H4** concentrations. The linear equation $Y = 0.5238X + 0.1046$ ($R^2 = 0.99$) and $Y = 0.2638X + 0.1216$ ($R^2 = 0.99$) was obtained for **CF-R9** and **CF-H4** respectively (Y = fluorescence intensity and X = concentration of **CF-R9** or **CF-H4**). Next, fluorescence intensity of carboxyfluorescein from the peptide-nanoparticle conjugates **CF-R9-CS** and **CF-H4-CS** was measured and the concentrations of **CF-R9** and **CF-H4** ($C_{pep}$) were determined using the above-mentioned calibration curve. Separately, the concentration of magnetic core particles $C_{core}$ was determined by using the volume fraction $\phi$ of maghemite $\gamma$-$Fe_2O_3$ ($C_{core} = \phi / (V_{part}.N_A)$, with $V_{part}$ being the average volume of a maghemite particle and $N_A$ the Avogadro's constant). Three maghemite cores are on average present in the same silica layer, the core-shell NP concentration $C_{CS}$ was then calculated by dividing the magnetic core concentration by three ($C_{CS} = C_{core} / 3$). Finally, the number of **CF-R9** and **CF-H4** peptides per core-shell NP was calculated from the ratio of concentration of **CF-R9/CF-H4** ($C_{pep}$) and concentration of core-shell NP ($C_{CS}$).

### 2.5 Cell culture

Wild type Chinese Hamster Ovary (CHO-K1) cells were cultured in DMEM-F12 culture medium supplemented with 10% fetal bovine serum (heat inactivated FBS), penicillin (100,000 IU/L), streptomycin (100,000 IU/L), and amphotericin B (1 mg/L) in a humidified atmosphere containing 5% $CO_2$ at 37 °C.

### 2.6 Live cell imaging of internalized nanoparticles

CHO-K1 cells were seeded in glass-bottom dishes treated beforehand with FBS for 1 h (10 000 cells/well in 200 μL DMEM-F12 containing 10% FBS, μ-Slide 8 Well ibiTreat). Cells were incubated at 37 °C in a 5% $CO_2$ atmosphere for 48 h before the medium was removed, and new medium containing the specified nanoparticles ([Fe] = 560 μM in 150 μL DMEM-F12) was added. The cells were incubated for a further 2 h or 6 h at 37 °C (for the 6 h incubation experiment, the medium was replaced after 4 h with fresh DMEM-F12 containing no nanoparticles). Cells were then washed twice with culture medium (200 μL) and three times with HBSS (200 μL) before Hoechst 33342 dye (4 μg per well) was added. After incubation for a further 15 min, cells were washed with culture medium (200 μL) before adding HBSS (200 μL). The cells were then immediately imaged on a Leica SP5 confocal microscope using a 63X oil immersion objective lens. When needed, trypan blue (100 μL) was added to the cells before imaging. Final images were generated as a maximum intensity projection of seven Z-stacked images (final image z = 0.9 μm) using FIJI ImageJ.[34] Pearson's correlation coefficient (PCC) values were obtained from coloc2 using FIJI ImageJ. Three representative cell images (> 30 cells) were used to calculate the PCC values, and the results are presented as mean ± standard deviation. The absolute PCC values of 1–0.7 indicate a relatively strong correlation, 0.69–0.36 indicate a moderate correlation.

## 2.7 Calcein leakage experiments

For monitoring calcein leakage, CHO-K1 cells were seeded in glass-bottom dishes treated beforehand with FBS for 1 h (10 000 cells/well in 200 μL DMEM-F12 containing 10% FBS, μ-Slide 8 Well ibiTreat). Cells were incubated at 37 °C in a 5% $CO_2$ atmosphere for 48 h, before the medium was removed. The cells were then incubated for 4 h with a new DMEM-F12 medium containing a mixture of the specified nanoparticles ([Fe] = 560 μM in 150 μL) and calcein (160 μM). The medium was then replaced with fresh DMEM-F12 containing no nanoparticles and the cells were incubated for a further 2 h. Treatment with calcein (160 $\mu$M in 150 $\mu$L) alone was also performed as a control. Cells were then processed and imaged as described above. Mean fluorescence intensity (MFI) was measured using FIJI ImageJ software. Three representative cell images with 10 nucleus/image were used to obtain the MFI for each condition. Data were expressed as mean ± standard deviation. Data were analyzed using one-way analysis of variance (ANOVA). ****P-value < 0.0001 was considered statistically significant. Statistical analysis was performed using the Prism software package (PRISM 8.0; GraphPad Software, USA).

## 2.8 LDH Cytotoxicity assay

Cytotoxicity was measured after 6 h or 24 h of cell incubation with the specified nanoparticles. CHO-K1 cells were seeded into 96-well flat bottom plates (15 000 cells/well for the 6 h cytotoxicity experiments, 5 000 cells/well for the 24 h cytotoxicity experiments). Cells were incubated at 37 °C in a 5% $CO_2$ atmosphere for 24 h before the medium was removed, and new medium (DMEM-F12) containing the specified nanoparticles at different iron concentration (0.14; 0.28; 0.56 and 1.12 mM in 60 $\mu$L) was added. For the 24 h cytotoxicity experiments, 50 $\mu$L of DMEM-F12 containing 5% FBS was added after 6 h cell incubation with the nanoparticles, and cells were incubated for further 18 h. At the end of the incubation times, LDH (Lactate dehydrogenase) release into cell media was analyzed using the CyQUANT™ LDH Cytotoxicity Assay Kit (Invitrogen) according to the manufacturer's protocol. In brief, each sample medium (50 $\mu$L) was transferred to a new 96-well flat bottom plate and the reaction mixture (50 $\mu$L) was added. After 30 min incubation, the stop solution (50 $\mu$L) was added and the absorbance was read at 490 nm and 680 nm. Controls (spontaneous LDH and maximum LDH activity) and percentage cytotoxicity calculations were conducted according to the manufacturer's protocol. Results were converted and represented as cell viability. Experiments were conducted in triplicate.

## 2.9 Transmission electron microscopy (TEM)

CHO-K1 cells were seeded in 12-well cell culture plates containing a 15 mm coverslip treated beforehand with FBS for 1 h (30 000 cells/well in 500 $\mu$L). Cells were incubated at 37 °C in a 5% $CO_2$ atmosphere for 48 h before the medium was removed, and new medium (DMEM-F12) containing the specified nanoparticles ([Fe] = 560 µM in 500 $\mu$L) was added. The cells were incubated for a further 6 h (the culture medium was replaced with fresh medium containing no nanoparticles after 4 h), then washed twice with culture medium (1 mL) and three times with HBSS (1 mL). The cells were fixed with glutaraldehyde (2%) in cacodylate buffer (0.1 M, pH 7.4) at RT for 2 h. The fixed cells were washed five times with cacodylate buffer (0.1 M, pH 7.4). Samples were then postfixed with 1% osmium tetroxide containing 1.5% potassium cyanoferrate (for membrane staining) on ice for 1 h, gradually dehydrated in ethanol (50% to 100%) and embedded in Agar 100 Epoxy resin. Thin sections (80 nm) were collected onto 200 mesh copper grids, and counterstained with uranyl acetate and lead citrate before examination in either conventional Transmission Electron Microscopy or Scanning Transmission Electron Microscopy (STEM-in-SEM). TEM was realized with a JEM-2100 (JEOL) operating at 80 kV with a LaB6 filament, and images were recorded with a side-mounted 2k x 2k Veleta CCD driven by iTEM software (Olympus). For STEM-in-SEM, counterstained grids were first coated with 2 nm carbon using ACE600 apparatus (Leica microsystems), before being imaged in STEM imaging mode within a Field-Emission Scanning Electron Microscope (FE-SEM) GeminiSEM 500 (Carl Zeiss Microscopy) operated at 20 kV, in bright field imaging mode with a 20 $\mu$m aperture (IBPS EM Facility, Sorbonne University, Paris, France).

## 2.10 Automatic acquisition in STEM-in-SEM and ultrastructural analysis

Previously observed TEM grids were automatically imaged in the STEM imaging mode of the GeminiSEM 500 SEM (20 kV, 20 $\mu$m aperture and high current mode) driven by Atlas 5 software (Carl Zeiss Microscopy). An automated mosaic process of acquisition (stitching of 25 adjacent ROI of 24.6 x 24.6 mm FOV) generated a large high-resolution map (FOV 100 x 100 mm, 1,7 Gpix, 3 nm / pixel). All images were acquired by mixing electrons collected simultaneously in Bright Field and in High Angular Annular Dark Field modes.

Two of these maps were examined for **CS** and for **CF-H4-CS**, representing more than 40 cells per condition. The nanoparticles were divided in 5 classes, depending on their location: endosome, multi-vesicular body (MVB), autophagosome, rupture of endosomal membrane, and cytosol. Two manual counting were realized using FIJI ImageJ software[34] and Cell Counter plugin (Total of events: 820 for **CS** and 834 for **CF-H4-CS**). Data were analyzed using the $\chi^2$ test of independence in Excel, according to the formula in the equation below ($A_{ij}$: observed values and $E_{ij}$ theoretical values):

$$\chi^2 = \sum\sum \frac{((A_{ij}) - E_{ij})^2}{E_{ij}}$$

## 3. RESULTS AND DISCUSSION

### 3.1 Strategy for the preparation of core-shell nanoparticles functionalized with peptides

Our strategy used the strain promoted azide-alkyne cycloaddition (SPAAC) for the conjugation of peptides onto the surface of $\gamma$-$Fe_2O_3$@$SiO_2$ core-shell nanoparticles (Figure 1). This required the installation of the two mutually reactive functional groups involved in the biorthogonal ligation (azide and strained alkyne) onto the peptide and nanoparticle precursors. The peptides and nanoparticles were labelled with different fluorophores (fluorescein and rhodamine respectively) to monitor the ligation reaction and to study the nanoparticle distribution inside cells by confocal microscopy. We opted to install the strained alkyne (DBCO) onto the nanoparticle and the azido group onto the peptide. This avoided the addition of an extra hydrophobic group to the peptide, thus limiting the risk of poor solubility and handling properties.

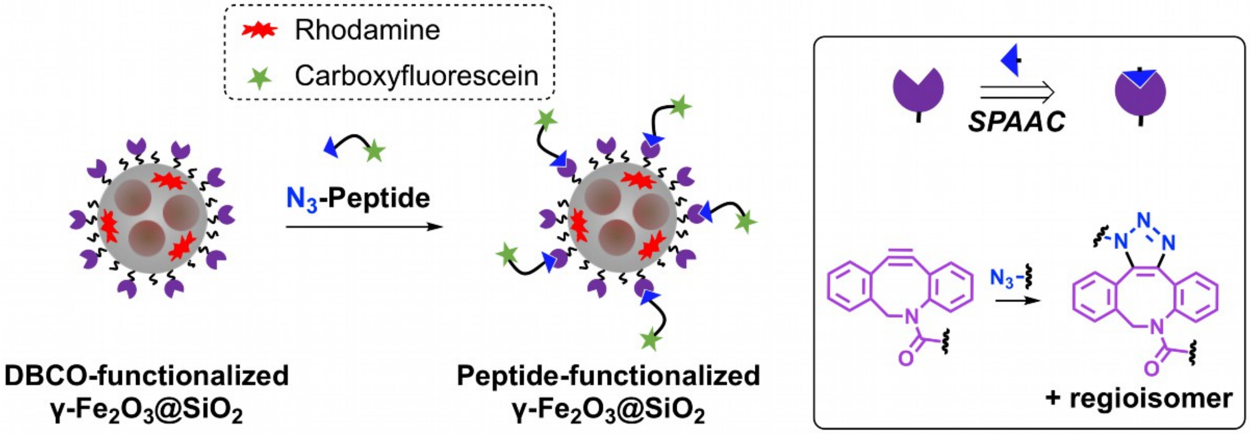

**Figure 1**. Click reaction between DBCO-functionalized core-shell nanoparticles and azido-functionalized peptides.

### 3.2 Synthesis and characterization of the azidopeptides

We started with the synthesis of the carboxyfluorescein (CF) labelled azidopeptides **CF-R9** (CF-Ahx-Lys(CO-$CH_2$-$N_3$)-$(Arg)_9$-$NH_2$) and **CF-H4** (CF-Ahx-Lys(CO-$CH_2$-$N_3$)-$(His)_4$-Trp-$NH_2$) (Figure 2a). The peptide segments $Arg_9$ and $His_4$-Trp (intermediates **1** and **2**) were first assembled using standard Fmoc solid phase peptide chemistry. Subsequently, a Lys residue orthogonally protected by an Alloc group was coupled to allow the later addition of an azido derivative on the Lys side chain. An aminohexanoic acid (Ahx) spacer was inserted prior to *N*-terminal functionalization with 5(6)-carboxyfluorescein to afford intermediates **3** and **4**. Selective Alloc removal from the lysine side chain was achieved by palladium catalyzed reductive deprotection to reveal the free amine, which was subsequently reacted with azidoacetic acid in the presence of DIC/HOBt. Both peptides were then fully deprotected and cleaved from the resin using standard TFA treatment, purified by reverse phase HPLC and characterized by MALDI-TOF mass spectrometry. The desired $[M+H]^+$ ion was observed for both **CF-R9** and **CF-H4** peptides (Figures 2b and S1). We also observed ion peaks (labelled by '◆', Figure 2b) corresponding to a loss of 28 compared to the expected m/z values, most likely due to fragmentation during MALDI-TOF MS analysis of the azido functionality resulting in the expulsion of $N_2$, as previously reported.[30]

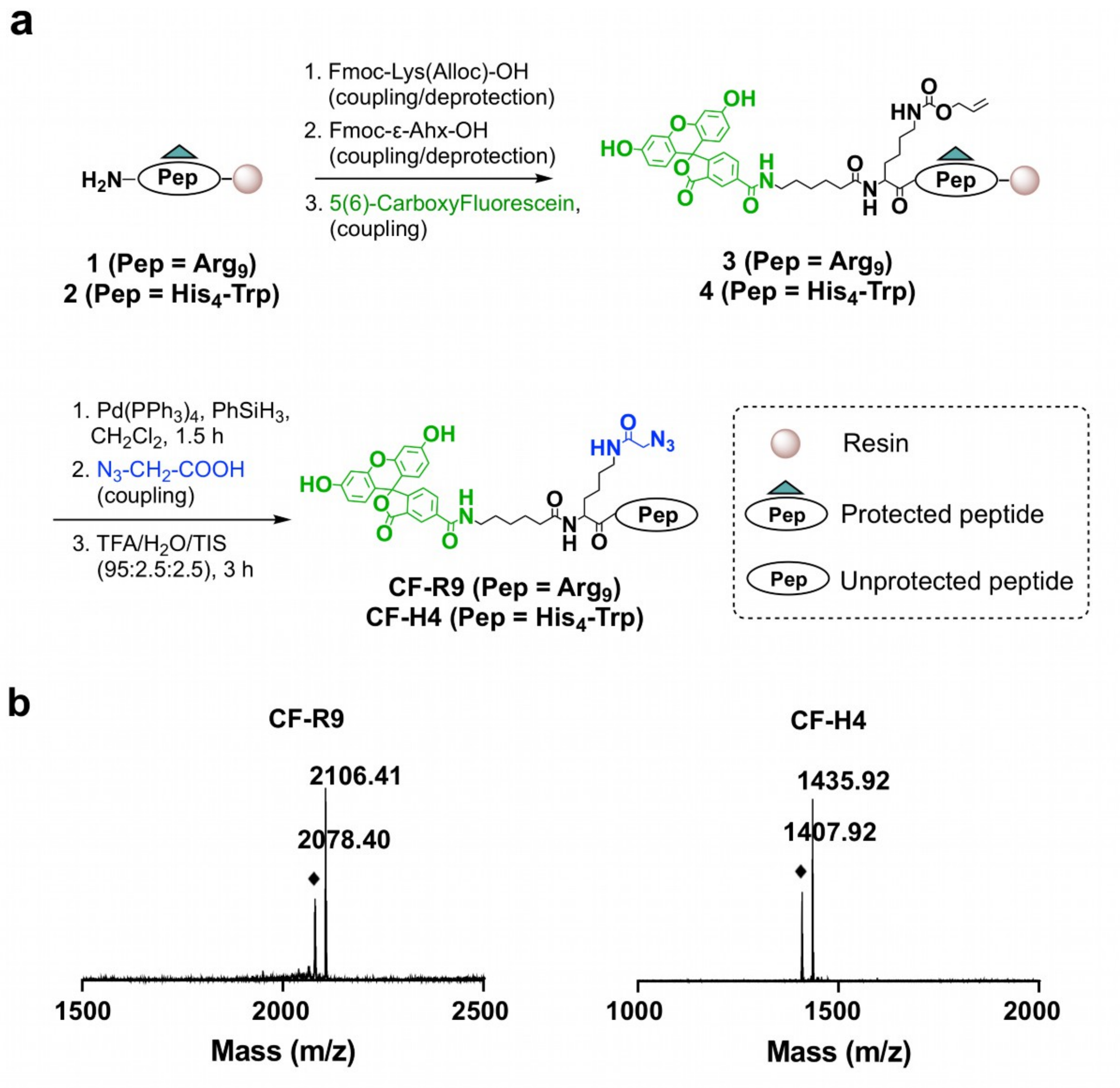

**Figure 2.** a) Synthesis of the azidopeptides **CF-R9** and **CF-H4**. Note that the peptides have a carboxamide function at their *C*-terminus. Pep = peptide, CF = 5(6)-carboxyfluorescein. b) MALDI-TOF mass spectra of **CF-R9** and **CF-H4**. Peaks labelled by ◆ correspond to a loss of 28 compared to the expected m/z values, presumably due to the expulsion of $N_2$ during MALDI-TOF MS analysis.

### 3.3 Synthesis and characterization of $\gamma$-$Fe_2O_3$@$SiO_2$ core-shell nanoparticles

Next, we moved onto the synthesis of rhodamine-labelled DBCO-functionalized nanoparticles **DBCO-CS** by adapting a previously reported procedure.[5] This approach employs amino groups grafted onto the surface of core-shell nanoparticles, that can readily undergo coupling with a *N*-hydroxysuccimidyl (NHS) activated DBCO (Figure 3a). The synthesis started with the preparation of magnetic nanoparticles (maghemite $\gamma$-$Fe_2O_3$) by alkaline co-precipitation of iron salts.[31] After size sorting, the average diameter of the magnetic cores was determined by TEM image analysis ($d_{TEM}$ = 11.1 nm, $\sigma$ = 0.17 nm, Figure S3) and their saturation magnetization ($M_S$) was measured with a Vibrating Sample Magnetometer (MS = 73.1 emu/g, Figure S4). The $\gamma$-$Fe_2O_3$ nanoparticle cores were then co-encapsulated with rhodamine in a thick silica shell by simultaneous treatment with tetraethoxysilane (TEOS) and APTS-rhodamine (Figure S5). Subsequent functionalization at the shell surface with short PEG chains and amino groups yielded $\gamma$-$Fe_2O_3$@$SiO_2$ core-shell nanoparticles **CS**. The average size of **CS** was measured by TEM image analysis (38.7 nm, $\sigma$ = 0.18 nm, average over 210 particles, Figure 3b, Table 1), which also confirmed the core-shell structure of the particles. The zeta potential of the **CS** nanoparticles was measured to be +22 mV (Table 1). The density of amino groups at the core-shell surface was determined by a fluorescamine assay (d= 2.0/$nm^2$, 3.4 mmol/L). In the final step, an NHS activated strained alkyne was coupled onto **CS** through the primary amine to produce **DBCO-CS**. A short $PEG_4$ linker was inserted to move the DBCO group away from the core-shell surface and thus increase their reactivity. The reaction conditions were optimized in terms of $NH_2$:NHS-$PEG_4$-DBCO molar ratio. The optimal molar ratio of $NH_2$:NHS-$PEG_4$-DBCO was found to be 10:1 for attaching **CF-R9** peptide and 20:1 for attaching **CF-H4** peptide, at which no aggregation of the nanoparticles was observed after conjugation to the peptides.

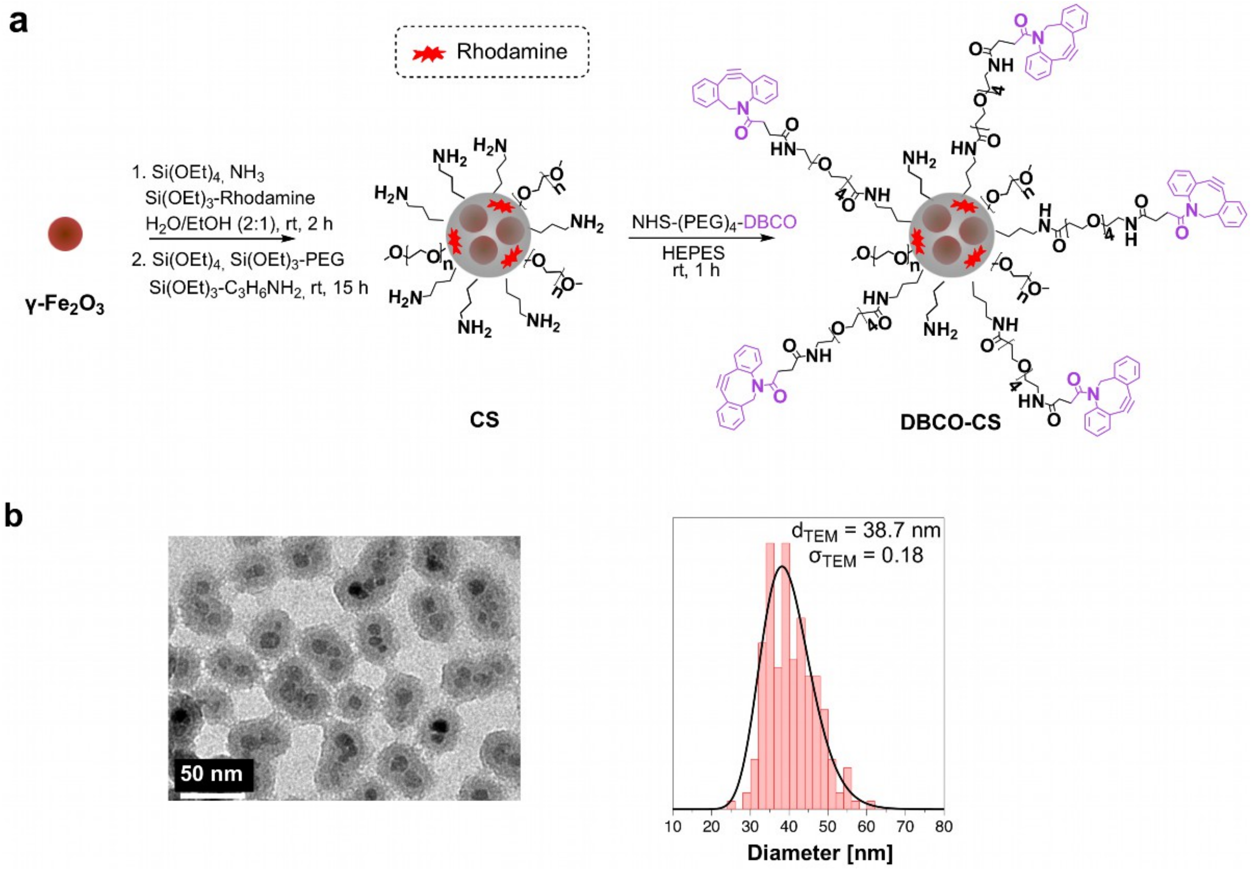

**Figure 3.** a) Preparation of DBCO-functionalized γ-$Fe_2O_3$@$SiO_2$ core-shell nanoparticles **DBCO-CS**. DBCO = dibenzocyclootyne. b) TEM image of **CS** and their size distribution. $d_{TEM}$ = average diameter of core-shell nanoparticles determined by TEM analysis.

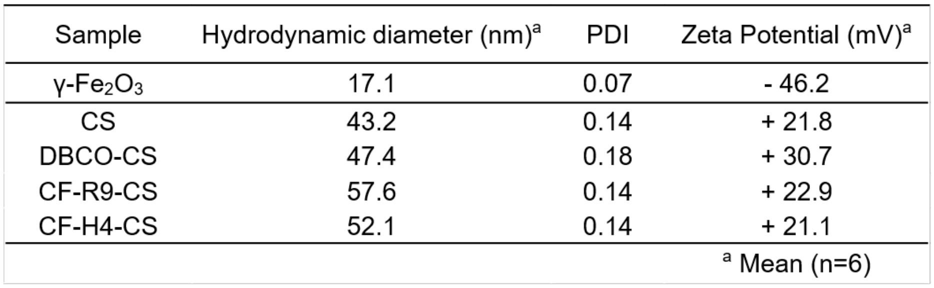

| Sample | Hydrodynamic diameter (nm)[a] | PDI | Zeta Potential (mV)[a] |
|---|---|---|---|
| γ-$Fe_2O_3$ | 17.1 | 0.07 | - 46.2 |
| CS | 43.2 | 0.14 | + 21.8 |
| DBCO-CS | 47.4 | 0.18 | + 30.7 |
| CF-R9-CS | 57.6 | 0.14 | + 22.9 |
| CF-H4-CS | 52.1 | 0.14 | + 21.1 |

[a] Mean (n=6)

**Table 1.** Summary of hydrodynamic diameter (analysis in number), polydispersity index (PDI), and zeta potential of the different nanoparticles, determined by DLS. The hydrodynamic size distributions of the core-shell nanoparticles are shown in Figure S6.

## 3.4 Functionalization of core-shell nanoparticles with cationic peptides by SPAAC click chemistry

With **CF-R9, CF-H4** peptides and **DBCO-CS** nanoparticles in hand, we applied the copper-free click reaction to generate the desired peptide-nanoparticle hybrids **CF-R9-CS** and **CF-H4-CS** by formation of a stable 1,2,3-triazole linkage (Figures 1 and 4a). Alkyne containing nanoparticles were treated with azidopeptides at a molar ratio of 2:1 (DBCO:$N_3$-Peptide) in HEPES buffer (pH 7.4). Initial attempts to purify the resulting peptide-nanoparticle conjugates by steric exclusion chromatography were unsuccessful due to the inefficient removal of non-covalently bound peptide. This was highlighted by imaging experiments using cells that had been incubated with the resulting sample **CF-R9-CS** (purified by steric exclusion chromatography). The images displayed weak colocalization between the rhodamine and carboxyfluorescein labels (See supplementary information Figure S7). The purification process was therefore changed to ultrafiltration (Nanosep, 10 kD) and applied to both **CF-R9-CS** and **CF-H4-CS**. The nanoparticle samples purified by ultrafiltration were then incubated with Chinese hamster ovary (CHO-K1) cells for 2 h. Confocal microscopy images showed this time an excellent colocalization of rhodamine and carboxyfluorescein, as confirmed by the calculated Pearson's colocalization coefficients[35] (PCC) (PCC = 0.94 ± 0.02 for **CF-R9-CS** and PCC = 0.91 ± 0.03 for **CF-H4-CS**, Figures 4 and S8). This indicated successful covalent functionalization of the core-shell nanoparticles with the peptides and also the complete removal of the unreacted peptide species. The conjugation of **CF-R9** or **CF-H4** peptides slightly increased the hydrodynamic diameter of the nanoparticles (**CF-R9-CS**= 58 nm, **CF-H4-CS**= 52 nm, Figure S6), without significantly affecting their zeta potential (Table 1). The polydispersity index remained below 0.2, indicating a narrow size distribution (Table 1). The quantity of peptides grafted onto the core-shell NPs was estimated by fluorescence spectroscopy to be 83 ± 3 and 76 ± 13 peptides per core-shell NPs for **CF-R9-CS** and **CF-H4-CS** respectively. It is worth noting that this quantity might be slightly underestimated due to self-quenching of the peptides close to each other at the surface of the CS.

This set of experiments confirmed that a covalent strategy is well suited when functionalizing $\gamma$-$Fe_2O_3$@$SiO_2$ core-shell nanoparticles with peptides (and in particular with CPPs, which can strongly interact with anionic components of the cell membrane), to avoid peptide premature release in the cellular context. These experiments also showed that the final step of nanoparticle purification to remove unreacted (non-covalently linked) peptides is particularly critical. Labeling the core-shell nanoparticles and the peptides with different fluorescent probes and analyzing their colocalization in cells was found to be very useful in optimizing the protocol of peptide grafting as well as assessing the purification efficiency of the final compounds.

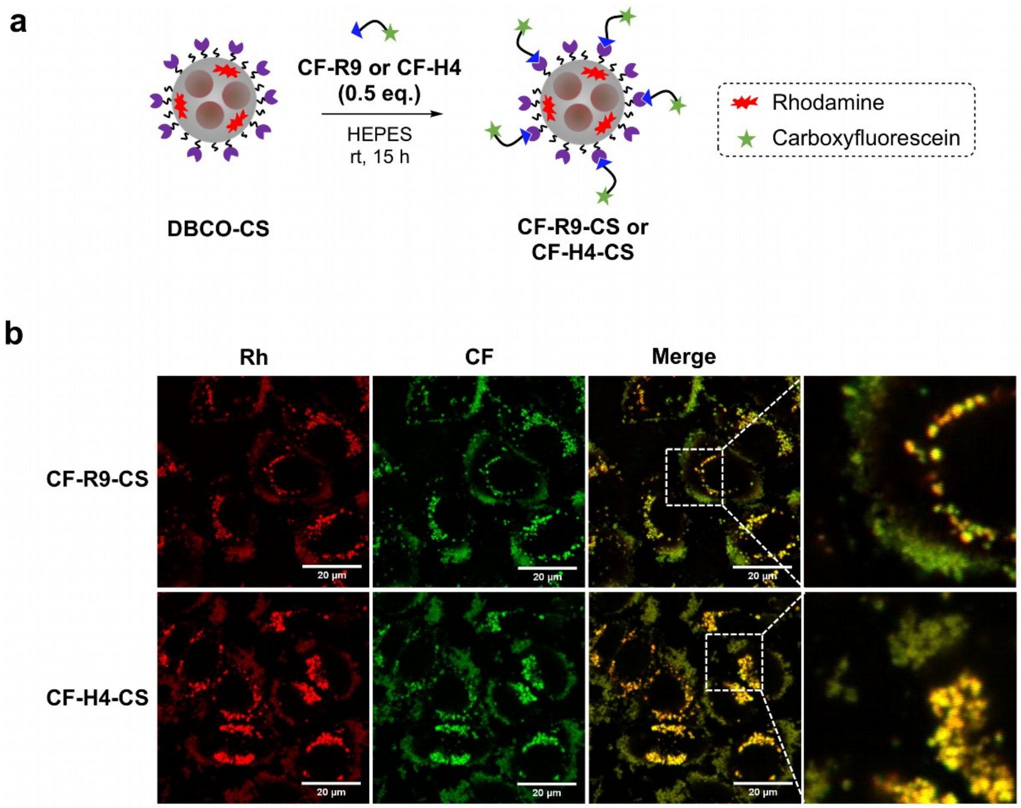

**Figure 4**. a) Click reaction between DBCO-functionalized core-shell nanoparticles **DBCO-CS** and azidopeptide **CF-R9** or **CF-H4**. b) Live cell confocal fluorescence microscopy images of CHO-K1 cells incubated for 2 h with **CF-R9-CS** or **CF-H4-CS** ([Fe] = 560 $\mu$M) in DMEM-F12 culture medium. Cells were washed twice with culture medium, thrice with HBSS before imaging. Rhodamine (Rh) is shown in red and carboxyfluorescein (CF) in green. Scale bars: 20 $\mu$m.

### 3.5 Simultaneous incorporation of mixed azido-substrates for the generation of bi-functionalized nanoparticles

Next, we explored the versatility of our functionalization method by incorporating two different substrates (**CF-R9** and cyanine5) onto the nanoparticle surface. **DBCO-CS** was first conjugated with **CF-R9** by using a higher DBCO:$N_3$-peptide ratio (4:1), the remaining DBCO sites were then reacted with cyanine5-azide (molar ratio of 4:1 (DBCO:Cy5-$N_3$) (Figure 5a). The successful addition of the two azido-substrates was confirmed by visualization of the dyes by confocal fluorescence microscopy after incubation of the CHO-K1 cells with the nanoparticles (Figure 5b). Good Pearson's correlation coefficient (PCC) values were measured between rhodamine/carboxyfluorescein ($PCC_{Rh/CF}$ = 0.76) and rhodamine/cyanine5 ($PCC_{Rh/Cy5}$ = 0.87), respectively, confirming the formation of the desired bi-functionalized nanoparticle conjugate **Cy5/CF-R9-CS** (Figure 5b). This proof of concept work demonstrates that our conjugation strategy is compatible with the addition of multiple substrates, and can be used for exploring the synergistic effect of attaching mixed functionalities/modalities to core-shell nanoparticles.

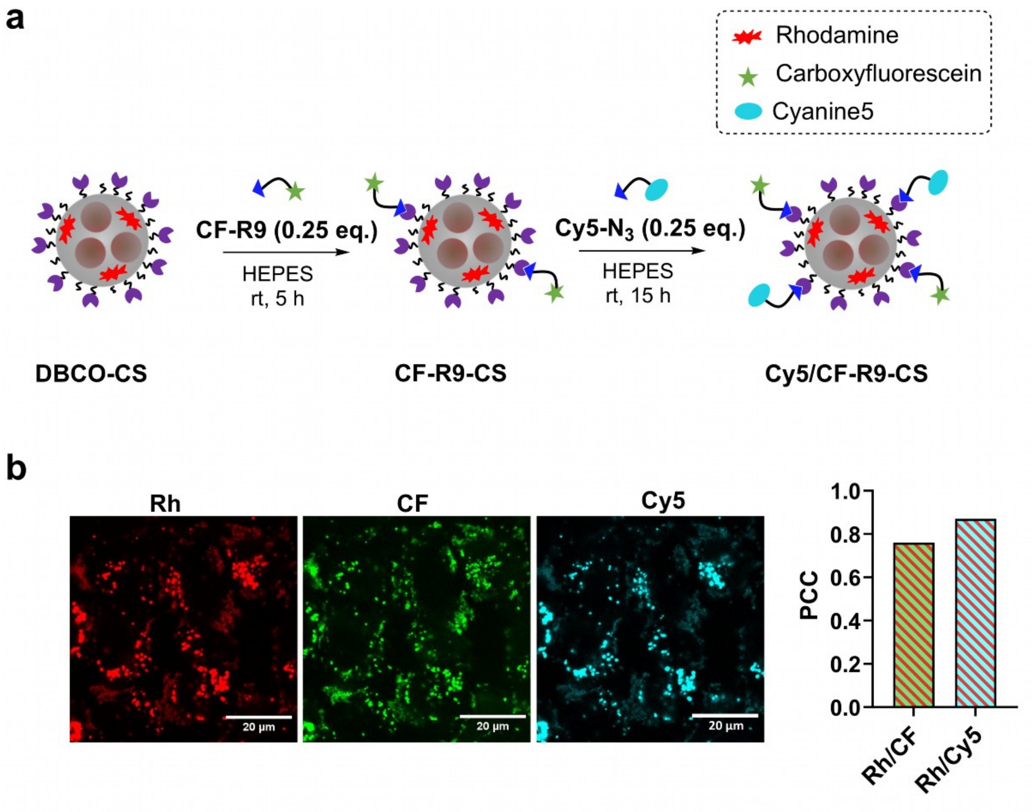

**Figure 5.** a) Bi-functionalization of **DBCO-CS** with **CF-R9** and Cy5-$N_3$ by click chemistry. b) Confocal fluorescence microscopy images of CHO-K1 cells incubated for 2 h with **Cy5/CF-R9-CS** ([Fe] = 560 $\mu$M) (live cell imaging) and measured PCC values. Rhodamine (Rh) is shown in red, carboxyfluorescein (CF) in green and cyanine5 (Cy5) in cyan. Scale bars: 20 $\mu$m.

## 3.6 Assessment of the intracellular distribution of the peptide-functionalized nanoparticles

### *3.6.1 Visualization of the fluorescently labelled conjugates by live cell confocal microscopy*

To investigate if conjugation of the cationic peptides can promote nanoparticle access to the cytosol, we analyzed the intracellular distribution of the functionalized core-shell nanoparticles **CF-R9-CS** and **CF-H4-CS** using live cell confocal fluorescence imaging. In the first experiments, cells were imaged directly after they were incubated with the nanoparticles for 2 h and washed with culture medium. This experiment showed for both **CF-R9-CS** and **CF-H4-CS,** appreciable levels of punctuate fluorescence surrounding the nucleus, as well as some diffuse fluorescence distributed within the cells (See supplementary information Figure S9a). In parallel, we also imaged cells that were treated with trypan blue after incubation with the nanoparticles in order to quench the fluorescence of membrane-bound species,[36] as the binding of nanoparticle conjugates to the cell membrane can result in misleading representations of their intracellular distribution. Trypan blue acts as a quenching agent for the green fluorescence of the carboxyfluorescein-labelled nanoparticle conjugates and because it does not enter cells by itself, it only quenches extracellular conjugates. However, the use of trypan blue prevents the visualization of the rhodamine fluorescence, due to overlapping of their fluorescence spectra. Upon direct comparison of images from trypan blue treated and untreated cells, we found similar levels of punctuate fluorescence suggestive of endosomal localization. In contrast, the diffuse fluorescence was no longer detectable for the trypan blue treated cells (See supplementary information Figure S9b). We concluded that the addition of trypan blue prior to imaging was a key step in obtaining an accurate representation of nanoparticle localization in cells and that after 2 h incubation, all internalized species were most likely present in endosomes. The absence of diffuse cytosolic fluorescence showed that both types of nanoparticles enter cells exclusively by endocytosis, the cationic peptides **CF-R9** and **CF-H4** were therefore unable to promote the direct translocation of the nanoparticle conjugates. Although the R9 CPP is known to enter cells by endocytosis and translocation, the extent of both pathways depends on the physicochemical properties of the CPP conjugates.[16] The increase in molecular size after core-shell NP conjugation (**CF-R9-CS** conjugate hydrodynamic diameter: 58 nm) is most likely an important contributing factor for the lack of NP cytosolic delivery by direct translocation. We reasoned that, if NP internalization occurred by endocytosis, a longer incubation time could enhance the levels of endosomal escape facilitated by the peptides. Pleasingly, after increasing the incubation period from 2 to 6 h, we were able to observe significant levels of a more diffuse intracellular fluorescence for the histidine functionalized nanoparticle **CF-H4-CS**, suggestive of endosomal escape (Figure 6 and see supplementary information Figure S10). In contrast, no change in the cellular localization was seen for the R9-linked conjugate.

As control experiments, unconjugated **CF-R9** and **CF-H4** peptides were incubated with cells and their intracellular distribution was analyzed (Figure S11). **CF-R9** gave strong punctuate and diffuse fluorescent signals, as expected from literature data.[22,24,37] In contrast, only a very weak punctuate fluorescent signal was observed for **CF-H4**, even after 6 h of incubation with cells, showing that the peptide is poorly internalized by endocytosis, and is unable to escape from endosomes. We speculate that the poor internalization of **CF-H4** is due to its weak ability to interact with the plasma membrane, as reported by Iwasaki and co-workers.[38] This may be attributed to the fact that the **CF-H4** peptide is not charged at the neutral extracellular pH. Taken together, our experiments suggest that a high concentration of His residues in endosomes is required to induce endosomal escape, this can be reached when the **CF-H4** peptide is conjugated to the core-shell nanoparticles.

In parallel to these experiments, we conducted a lactate dehydrogenase (LDH) release assay after 6 and 24 h of incubation. This assay measures the cytotoxicity by quantifying the release of the cytosolic enzyme LDH into the extracellular environment upon damage to the plasma membrane. The LDH assay showed that the nanoparticle conjugates did not induce any general cytotoxicity in CHO-K1 cells after 6 or 24 h of incubation (See supplementary information Figure S12).

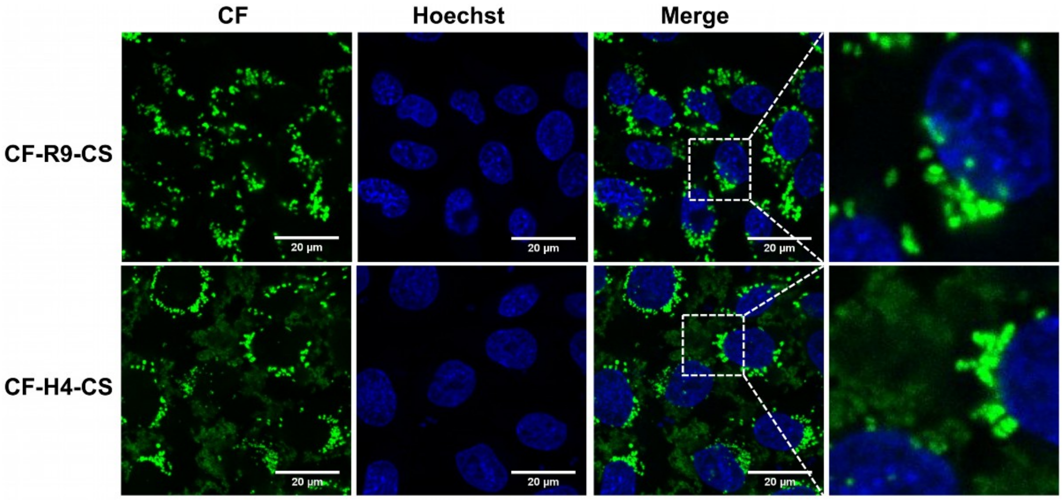

**Figure 6.** Confocal fluorescence microscopy images of CHO-K1 cells incubated for 6 h with **CF-R9-CS** or **CF-H4-CS** ([Fe] = 560 μM) and then treated with trypan blue (live cell imaging). Carboxyfluorescein (CF) is shown in green and Hoechst dye in blue. Scale bars: 20 μm.

### *3.6.2 Visualization of intracellular calcein distribution by live cell confocal microscopy*

We further investigated the capabilities of **CF-H4-CS** at inducing endosomal escape by tracking the intracellular distribution of co-incubated calcein. This method has previously been used to evaluate the ability of nanomaterials to disrupt the membrane of endocytic vesicles.[28,39,40] When incubated alone with cells, the green fluorescent calcein dye is internalized *via* the endocytic pathway and largely found trapped in endosomes. The release of calcein from the endosomes can be used as an indirect measure of vesicle disruption caused by an external stimulus.[41] To avoid competition when visualizing the green fluorescence of calcein, we synthesized peptides **R9*** and **H4***, which are non-fluorescent versions of our cationic azidopeptides (Figure 7a). Both peptides were subsequently conjugated to the core-shell nanoparticles. The resulting hybrids **R9*-CS** and **H4*-CS** were then co-incubated with calcein for 6 h in CHO-K1 cells. Analysis of the calcein distribution by live cell confocal microscopy showed that only cells treated with **H4*-CS** displayed significant diffuse fluorescence throughout the cell (suggestive of calcein presence in the cytosol and nucleus), whereas treatment with **R9*-CS** or **CS** alone resulted in only punctuate cytoplasmic fluorescence (Figure 7b). We confirmed this observation by quantifying the mean fluorescence intensity observed in the nucleus upon incubation with the different nanoparticle conjugates, our results show a clear improvement for cells treated with histidine-bound nanoparticles (Figure 7c, control experiments were carried out with treatment of calcein alone). Our data strongly suggest a simultaneous internalization *via* endocytosis of calcein and nanoparticles (as confirmed by co-localization of calcein/rhodamine by live cell confocal fluorescence microscopy, see supplementary information Figure S13), which was followed by endosomal escape promoted by the tetra-histidine motif resulting in calcein redistribution into the cytosol and nucleus.

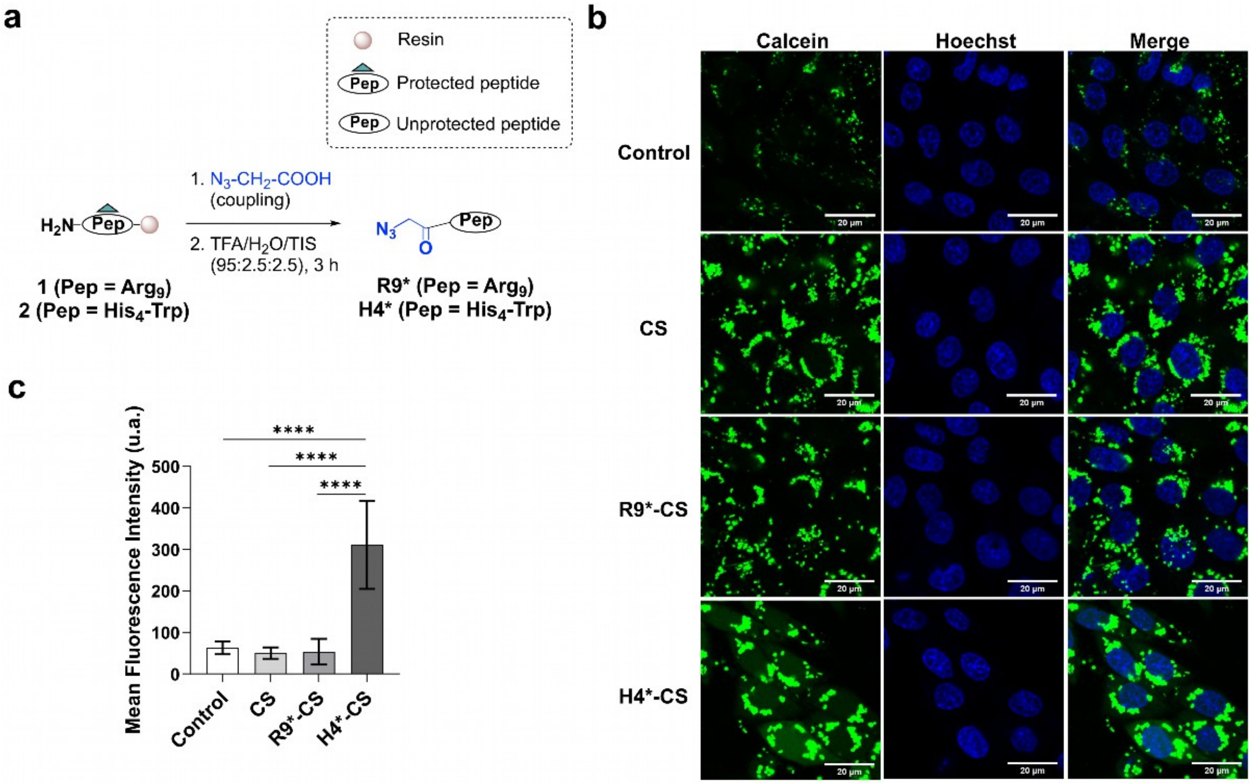

**Figure 7**. a) Synthesis of the azidopeptides **R9*** ($N_3$-$CH_2$-CO-$(Arg)_9$-$NH_2$) and **H4*** ($N_3$-$CH_2$-CO-$(His)_4$-Trp-$NH_2$). Pep = peptide. b) Confocal fluorescence microscopy images of CHO-K1 cells co-incubated for 6 h with calcein (160 $\mu$M) and **CS**, **R9*-CS** or **H4*-CS** ([Fe] = 560 $\mu$M) and then treated with trypan blue (live cell imaging). A control experiment was performed in the same conditions but with calcein alone (160 $\mu$M). Calcein is shown in green and Hoechst dye in blue. Scale bars: 20 $\mu$m. c) Corresponding mean fluorescence intensity of calcein found in the nucleus. Data are represented as mean ± SD (n = 30). ****: $p < 0.0001$.

### *3.6.3 Direct visualization of the intracellular localization of the core-shell nanoparticles using transmission electron microscopy*

Finally, we performed transmission electron microscopy (TEM) and scanning transmission electron microscopy (STEM-in-SEM) on thin sections of fixed cells incubated with the different nanoparticles. This technique can provide higher resolution images compared to confocal microscopy. It also allows the direct identification of cellular organelles and to more precisely observe the NP localization in cells. Cellular membranes were stained with potassium ferrocyanide-reduced osmium (according to Karnovsky's protocol[42]) to allow the observation of potentially damaged endosomes. TEM and STEM images show that the majority of internalized nanoparticles were localized in enlarged endosomes (Figure 8), as previously reported by Di Corato *et al*. for different nanoparticles.[3] Interestingly, events of endosomal membrane rupturewere observed in the TEM images. More specifically, we were able to visualize nanoparticles being released from zones of damaged endosomes with no visible membrane surrounding (white arrows in Figure 8). Importantly, we observed more endosomal membrane rupture events for cells incubated with the histidine functionalized nanoparticles **CF-H4-CS**, as compared to **CF-R9-CS** and **CS** (Figure 8). This is in good agreement with our data obtained by confocal microscopy suggesting the poly-His is able to promote endosomal escape of core-shell nanoparticles.

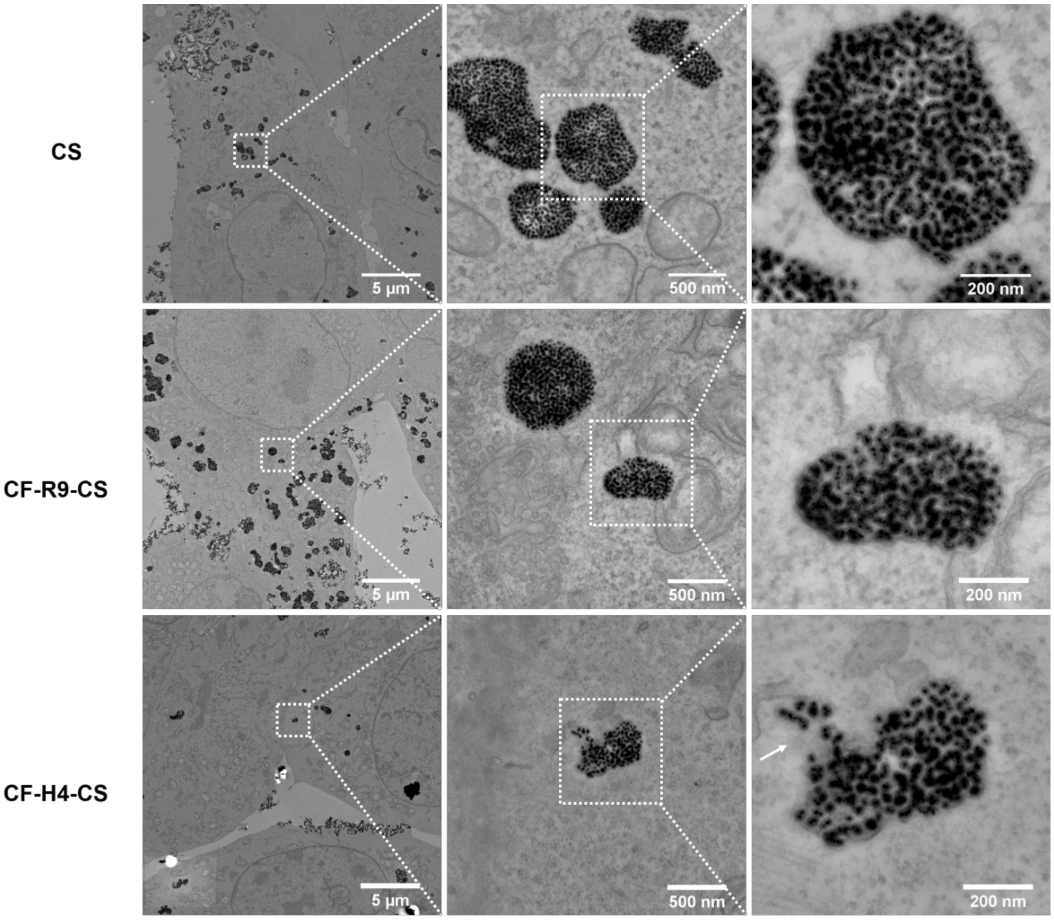

**Figure 8**. STEM-in-SEM images of CHO-K1 cells incubated with **CS**, **CF-R9-CS** or **CF-H4-CS** ([Fe] = 560 $\mu$M) for 6 h. The zoom images show **CS** and **CF-R9-CS** nanoparticles encapsulated in intact endosomes and **CF-H4-CS** nanoparticles escaping from damaged endosomes (in this later case the endosomal membrane is discontinuous, the white arrow points the membrane rupture zone).

To confirm these preliminary observations, we automatized sample acquisitions using STEM-in-SEM to extensively classify and quantify events associated to the nanoparticles, according to the nanoparticle intracellular localizations. These experiments were performed for cells incubated with **CS** and **CF-H4-CS** (Figure 9). Importantly, we did not observe any evidence of mislocalization of NPs caused by sample preparation (e.g., NPs on a different focal plan or holes in the sections, both made by a displacement of NPs during ultramicrotomy). In addition, the image contrast was optimized to avoid any misinterpretation. We were able to distinguish five different situations in the STEM images NPs were detected in: 1) intact early endosomes, 2) intact late endosomes/multi-vesicular bodies, 3) intact autophagosomes, 4) damaged endosomal vesicles upon membrane rupture (local absence of membrane was observed) and 5) free in the cytosol (Figure 9). We observed that the NPs free in the cytosol appeared to remain in clusters although there are no membranes sequestering them. This phenomenon may be attributed to the high ionic strength and high viscosity of the cytosolic medium.

More than 800 events were classified into these 5 families for cells incubated with **CS** or with **CF-H4-CS** and the distributions are shown Figure 9b (see also Table **S1**). The analysis of the different internalization events showed a significant difference between the intracellular distributions of **CS** and **CF-H4-CS** ($\chi^2$ test of independence, $p < 3.10^{-13}$). Both “Free NPs” and “Endosomal Rupture” types of event contribute towards NPs that have cytosolic access, the large majority being found in damaged endosomes. Importantly, we observed a significant 1.7-fold increase in ‘Endosomal Rupture’ for cells incubated with **CF-H4-CS** as compared to **CS** (**CF-H4-CS**: 33% *vs* **CS**: 20%, Figure 9b), further proving that NPs functionalized with the poly-histidine peptide can more effectively access the cytosol.

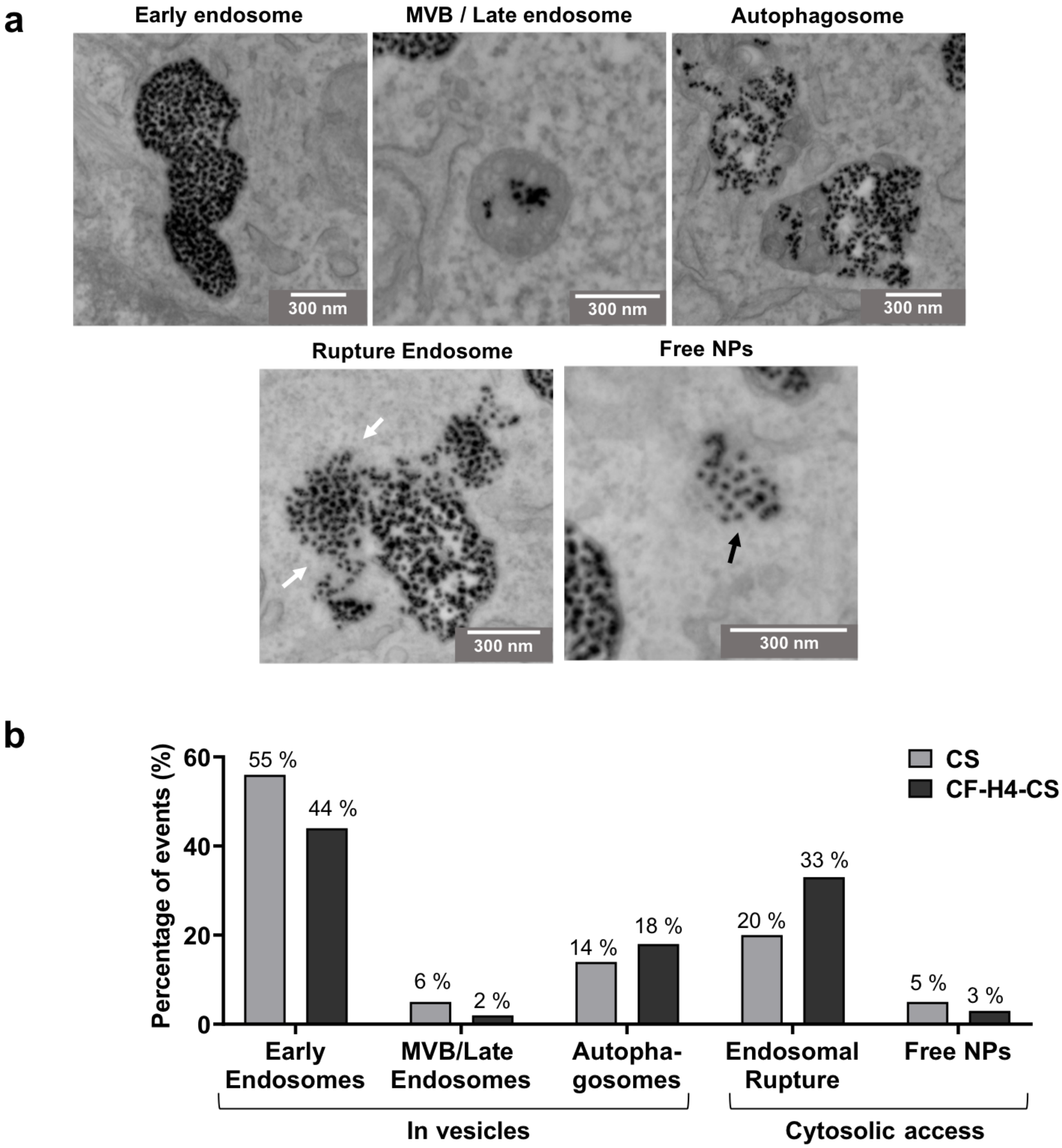

**Figure 9**. STEM analysis of ultrathin sections of cells incubated with **CS** or **CF-H4-CS** ([Fe] = 560 $\mu$M) for 6 h. **a)** Representative examples of STEM images showing: i) NPs in intact early endosomes (EE), ii) NPs in intact multi-vesicular bodies (MVB)/late endosomes (LE) (both characterized by the presence of intraluminal vesicles), iii) NPs in intact autophagosomes (characterized by a double membrane), iv) NPs escaping from endosomes showing a rupture of

their membrane (white arrows) and v) NPs free in the cytosol (black arrow). Scale bars: 300 nm. **b)** Intracellular distribution of the nanoparticles. More than 800 events were analyzed per conditions. Noteworthy each event represents an assembly of NPs, the number of NPs present within each assembly was not counted. A $\chi^2$ test of independence was performed showing a high significance difference between the distributions of **CS1** and **CF-H4-CS1**: $\chi^2 = 64.44$, df 4, $p < 3.10^{-13}$.

## CONCLUSIONS

We have reported in this study a robust procedure to functionalize $Fe_2O_3@SiO_2$ core-shell nanoparticles with cationic peptides, using click chemistry. Both starting materials used in the click reaction, core-shell nanoparticles and peptides were labeled with fluorophores. Their successful covalent conjugation was confirmed by fluorescence microscopy after incubation of the resulting functionalized nanoparticles with cells. Using this procedure, we were able to prepare well-defined and stable nanoparticles conjugated to a poly-arginine (**CF-R9**) or a poly-histidine (**CF-H4**) peptide.

By combining complementary techniques (live cells fluorescence confocal microscopy, calcein endosomal release experiments and ultrastructural analysis in TEM), we were able to analyze the process of cellular uptake of the nanoparticles and define their intracellular distribution. Over short incubation times (2 h), peptide-functionalized NPs (**CF-R9-CS** and **CF-H4-CS)** were found to enter cells *via* endocytosis. However, over longer incubation periods (6 h) we observed cytosolic localization for **CF-H4-CS**. In stark contrast, only endosomal fluorescence was visualized for cells incubated with **CF-R9-CS** or with unconjugated **CS**. Interestingly, the faint cytosolic fluorescent signal observed for **CF-H4-CS** was not uniform. This is likely due to the fact that the NPs, even when free in the cytosol, remain clustered, as observed in the TEM images.

We further confirmed the ability of poly-histidine functionalized nanoparticles to facilitate endosomal membrane damage through a calcein release assay. Importantly, ultrastructural images from TEM and STEM were used to provide a more accurate localization analysis of the nanoparticles, confirming the capability of the **CF-H4-CS** nanoparticles to escape from endosomes. The His-rich peptide was therefore able to trigger a disruption of the endosomal membrane, possibly by the mechanism of proton sponge, as proposed in the literature.[25–28] Efficient uptake by endocytosis, leading to a high concentration of His residues in endosomes appears to be required for this process to occur. This was achieved by covalent conjugation of the His-rich peptide to the core-shell nanoparticles. Cellular viability assays demonstrated that the process of endosomal escape of **CF-H4-CS** did not induce any associated toxicity.

Endosomal escape is currently a critical bottleneck in therapeutic delivery of nanoparticles. Further development of the approach developed in this study will focus on assessing if endosomal escape can provide a significant therapeutic gain. Such evaluation can be achieved by grafting a cytosol-targeted therapeutic molecule to the surface of the core-shell nanoparticles. The versatility of our strategy is well placed for such future development, as demonstrated by the ability to introduce multiple substrates onto the nanoparticle surface.

Alternative applications can involve attaching a ligand to the NP that targets an intracellular protein, allowing their magnetic manipulation in the cytosol to trigger a signalization pathway. Such signalization pathway could also be activated by the heat generated by the magnetic nanoparticles when subjected to an alternative magnetic field. It is important to note that for this type of cellular engineering application, it is not necessary to have a high concentration of NPs in the cytosol. The simplicity and versatility of the click-chemistry and the non-toxicity of the conjugates **CF-H4-CS** coupled with their capacity to facilitate endosomal escape make them promising tools for magnetic cellular engineering.

## ASSOCIATED CONTENT

### Supporting Information

The Supporting Information is available free of charge on the ACS Publications website at DOI:

**Figures S1, S2. Peptide characterization:** Analytical HPLC chromatograms and MALDI-TOF mass spectra. **Figures S3 – S6. Magnetic nanoparticles characterization:** TEM image, magnetization curve, fluorescence emission spectrum and size distribution. Figures **S7, S8. Assessment of peptide-nanoparticle conjugation:** Fluorescence microscopy images on fixed cells and Pearson's correlation coefficient (PCC) values. Figures **S9 – S13,** Table **S1. Intracellular distribution and cytotoxicity studies:** Live cell confocal fluorescence microscopy images, LDH release assay and STEM images analysis.

## AUTHOR INFORMATION

### Corresponding Author

*Email: christine.menager@sorbonne-universite.fr / fabienne.burlina@sorbonne-universite.fr

### ORCID

### Author Contributions

The manuscript was written through contributions of all authors. All authors have given approval to the final version of the manuscript.

### Notes

The authors declare no competing financial interests.

## ACKNOWLEDGMENT

We thank Gilles Clodic for the MALDI-TOF MS analysis (MS3U platform, Sorbonne Université - CNRS, UFR 926, UFR 927) as well as Christophe Piesse for microwave-assisted SPPS (Plateforme d'ingénierie des protéines, service synthèse peptidique de l'IBPS, Sorbonne Université). We thank Photon microscopy facility IBPS (Sorbonne Université) for assistance with confocal microscopy. We thank Alexis Canette (Electron microscopy facility IBPS, Sorbonne Université) for its work on automatic STEM-in-SEM imaging. Dr. Mathilde Le Jeune was financially supported by the French Ministère de l'Enseignement Supérieur de la Recherche et de l'Innovation (M.E.S.R.I.) within the Programme Interfaces pour le vivant (IPV).

## REFERENCES

(1) Cardoso, V. F.; Francesko, A.; Ribeiro, C.; Bañobre-López, M.; Martins, P.; Lanceros-Mendez, S. Advances in Magnetic Nanoparticles for Biomedical Applications. *Adv. Healthc. Mater.* **2018**, *7* (5), 1700845. https://doi.org/10.1002/adhm.201700845.

(2) Monzel, C.; Vicario, C.; Piehler, J.; Coppey, M.; Dahan, M. Magnetic Control of Cellular Processes Using Biofunctional Nanoparticles. *Chem. Sci.* **2017**, *8* (11), 7330–7338. https://doi.org/10.1039/C7SC01462G.

(3) Di Corato, R.; Espinosa, A.; Lartigue, L.; Tharaud, M.; Chat, S.; Pellegrino, T.; Ménager, C.; Gazeau, F.; Wilhelm, C. Magnetic Hyperthermia Efficiency in the Cellular Environment for Different Nanoparticle Designs. *Biomaterials* **2014**, *35* (24), 6400–6411. https://doi.org/10.1016/j.biomaterials.2014.04.036.

(4) Cabrera, D.; Coene, A.; Leliaert, J.; Artés-Ibáñez, E. J.; Dupré, L.; Telling, N. D.; Teran, F. J. Dynamical Magnetic Response of Iron Oxide Nanoparticles Inside Live Cells. *ACS Nano* **2018**, *12* (3), 2741–2752. https://doi.org/10.1021/acsnano.7b08995.

(5) Schöneborn, H.; Raudzus, F.; Secret, E.; Otten, N.; Michel, A.; Fresnais, J.; Ménager, C.; Siaugue, J.-M.; Zaehres, H.; Dietzel, I. D.; Heumann, R. Novel Tools towards Magnetic Guidance of Neurite Growth: (I) Guidance of Magnetic Nanoparticles into Neurite Extensions of Induced Human Neurons and In Vitro Functionalization with RAS Regulating Proteins. *J. Funct. Biomater.* **2019**, *10* (3), 32. https://doi.org/10.3390/jfb10030032.

(6) Raudzus, F.; Schöneborn, H.; Neumann, S.; Secret, E.; Michel, A.; Fresnais, J.; Brylski, O.; Ménager, C.; Siaugue, J.-M.; Heumann, R. Magnetic Spatiotemporal Control of SOS1 Coupled Nanoparticles for Guided Neurite Growth in Dopaminergic Single Cells. *Sci. Rep.* **2020**, *10* (1), 22452. https://doi.org/10.1038/s41598-020-80253-w.

(7) Etoc, F.; Vicario, C.; Lisse, D.; Siaugue, J.-M.; Piehler, J.; Coppey, M.; Dahan, M. Magnetogenetic Control of Protein Gradients Inside Living Cells with High Spatial and Temporal Resolution. *Nano Lett.* **2015**, *15* (5), 3487–3494. https://doi.org/10.1021/acs.nanolett.5b00851.

(8) Etoc, F.; Lisse, D.; Bellaiche, Y.; Piehler, J.; Coppey, M.; Dahan, M. Subcellular Control of Rac-GTPase Signalling by Magnetogenetic Manipulation inside Living Cells. *Nat. Nanotechnol.* **2013**, *8* (3), 193–198. https://doi.org/10.1038/nnano.2013.23.

(9) Bolhassani, A.; Jafarzade, B. S.; Mardani, G. In Vitro and in Vivo Delivery of Therapeutic Proteins Using Cell Penetrating Peptides. *Peptides* **2017**, *87*, 50–63. https://doi.org/10.1016/j.peptides.2016.11.011.

(10) McClorey, G.; Banerjee, S. Cell-Penetrating Peptides to Enhance Delivery of Oligonucleotide-Based Therapeutics. *Biomedicines* **2018**, *6* (2), 51. https://doi.org/10.3390/biomedicines6020051.

(11) Fischer, R.; Fotin-Mleczek, M.; Hufnagel, H.; Brock, R. Break on through to the Other Side-Biophysics and Cell Biology Shed Light on Cell-Penetrating Peptides. *ChemBioChem* **2005**, *6* (12), 2126–2142. https://doi.org/10.1002/cbic.200500044.

(12) Stanzl, E. G.; Trantow, B. M.; Vargas, J. R.; Wender, P. A. Fifteen Years of Cell-Penetrating, Guanidinium-Rich Molecular Transporters: Basic Science, Research Tools, and Clinical Applications. *Acc. Chem. Res.* **2013**, *46* (12), 2944–2954. https://doi.org/10.1021/ar4000554.

(13) Futaki, S.; Nakase, I. Cell-Surface Interactions on Arginine-Rich Cell-Penetrating Peptides Allow for Multiplex Modes of Internalization. *Acc. Chem. Res.* **2017**, *50* (10), 2449–2456. https://doi.org/10.1021/acs.accounts.7b00221.

(14) Walrant, A.; Cardon, S.; Burlina, F.; Sagan, S. Membrane Crossing and Membranotropic Activity of Cell-Penetrating Peptides: *Dangerous Liaisons* ? *Acc. Chem. Res.* **2017**, *50* (12), 2968–2975. https://doi.org/10.1021/acs.accounts.7b00455.

(15) Guidotti, G.; Brambilla, L.; Rossi, D. Cell-Penetrating Peptides: From Basic Research to Clinics. *Trends Pharmacol. Sci.* **2017**, *38* (4), 406–424. https://doi.org/10.1016/j.tips.2017.01.003.

(16) Gessner, I.; Neundorf, I. Nanoparticles Modified with Cell-Penetrating Peptides: Conjugation Mechanisms, Physicochemical Properties, and Application in Cancer Diagnosis and Therapy. *Int. J. Mol. Sci.* **2020**, *21* (7), 2536. https://doi.org/10.3390/ijms21072536.

(17) Dalal, C.; Jana, N. R. Multivalency Effect of TAT-Peptide-Functionalized Nanoparticle in Cellular Endocytosis and Subcellular Trafficking. *J. Phys. Chem. B* **2017**, *121* (14), 2942–2951. https://doi.org/10.1021/acs.jpcb.6b12182.

(18) Ding, C.; Wu, K.; Wang, W.; Guan, Z.; wang, L.; Wang, X.; Wang, R.; Liu, L.; Fan, J. Synthesis of a Cell Penetrating Peptide Modified Superparamagnetic Iron Oxide and MRI Detection of Bladder Cancer. *Oncotarget* **2017**, *8* (3), 4718–4729. https://doi.org/10.18632/oncotarget.13578.

(19) Lee, J. S.; Tung, C.-H. Enhancing the Cellular Delivery of Nanoparticles Using Lipo-Oligoarginine Peptides. *Adv. Funct. Mater.* **2012**, *22* (23), 4924–4930. https://doi.org/10.1002/adfm.201201345.

(20) Ben Djemaa, S.; Hervé-Aubert, K.; Lajoie, L.; Falanga, A.; Galdiero, S.; Nedellec, S.; Soucé, M.; Munnier, E.; Chourpa, I.; David, S.; Allard-Vannier, E. GH625 Cell-Penetrating Peptide Promotes the Endosomal Escape of Nanovectorized SiRNA in a Triple-Negative Breast Cancer Cell Line. *Biomacromolecules* **2019**, *20* (8), 3076–3086. https://doi.org/10.1021/acs.biomac.9b00637.

(21) Sun, P.; Huang, W.; Kang, L.; Jin, M.; Fan, B.; Jin, H.; Wang, Q.; Gao, Z. SiRNA-Loaded Poly(Histidine-Arginine)$_6$-Modified Chitosan Nanoparticle with Enhanced Cell-Penetrating and Endosomal Escape Capacities for Suppressing Breast Tumor Metastasis. *Int. J. Nanomedicine* **2017**, *Volume 12*, 3221–3234. https://doi.org/10.2147/IJN.S129436.

(22) Mitchell, D. J.; Steinman, L.; Kim, D. T.; Fathman, C. G.; Rothbard, J. B. Polyarginine Enters Cells More Efficiently than Other Polycationic Homopolymers: Cellular Uptake of Polyarginine. *J. Pept. Res.* **2000**, *56* (5), 318–325. https://doi.org/10.1034/j.1399-3011.2000.00723.x.

(23) Futaki, S.; Suzuki, T.; Ohashi, W.; Yagami, T.; Tanaka, S.; Ueda, K.; Sugiura, Y. Arginine-Rich Peptides. An Abundant Source of Membrane-Permeable Peptides Having Potential as Carriers for Intracellular Protein Delivery. *J. Biol. Chem.* **2001**, *276* (8), 5836–5840. https://doi.org/10.1074/jbc.M007540200.

(24) Jiao, C.-Y.; Delaroche, D.; Burlina, F.; Alves, I. D.; Chassaing, G.; Sagan, S. Translocation and Endocytosis for Cell-Penetrating Peptide Internalization. *J. Biol. Chem.* **2009**, *284* (49), 33957–33965. https://doi.org/10.1074/jbc.M109.056309.

(25) Wolf, J.; Aisenbrey, C.; Harmouche, N.; Raya, J.; Bertani, P.; Voievoda, N.; Süss, R.; Bechinger, B. PH-Dependent Membrane Interactions of the Histidine-Rich Cell-Penetrating Peptide LAH4-L1. *Biophys. J.* **2017**, *113* (6), 1290–1300. https://doi.org/10.1016/j.bpj.2017.06.053.

(26) Bilalis, P.; Tziveleka, L.-A.; Varlas, S.; Iatrou, H. PH-Sensitive Nanogates Based on Poly( L -Histidine) for Controlled Drug Release from Mesoporous Silica Nanoparticles. *Polym. Chem.* **2016**, *7* (7), 1475–1485. https://doi.org/10.1039/C5PY01841B.

(27) Li, Q.; Hao, X.; Zaidi, S. S. A.; Guo, J.; Ren, X.; Shi, C.; Zhang, W.; Feng, Y.

Oligohistidine and Targeting Peptide Functionalized TAT-NLS for Enhancing Cellular Uptake and Promoting Angiogenesis in Vivo. *J. Nanobiotechnology* **2018**, *16* (1), 29. https://doi.org/10.1186/s12951-018-0358-x.

(28) Gisbert-Garzarán, M.; Lozano, D.; Matsumoto, K.; Komatsu, A.; Manzano, M.; Tamanoi, F.; Vallet-Regí, M. Designing Mesoporous Silica Nanoparticles to Overcome Biological Barriers by Incorporating Targeting and Endosomal Escape. *ACS Appl. Mater. Interfaces* **2021**, *13* (8), 9656–9666. https://doi.org/10.1021/acsami.0c21507.

(29) Takayama, Y.; Kusamori, K.; Nishikawa, M. Click Chemistry as a Tool for Cell Engineering and Drug Delivery. *Molecules* **2019**, *24* (1), 172. https://doi.org/10.3390/molecules24010172.

(30) Li, Y.; Hoskins, J. N.; Sreerama, S. G.; Grayson, S. M. MALDI–TOF Mass Spectral Characterization of Polymers Containing an Azide Group: Evidence of Metastable Ions. *Macromolecules* **2010**, *43* (14), 6225–6228. https://doi.org/10.1021/ma100599n.

(31) Massart, R.; Dubois, E.; Cabuil, V.; Hasmonay, E. Preparation and Properties of Monodisperse Magnetic Fluids. *J. Magn. Magn. Mater.* **1995**, *149* (1–2), 1–5. https://doi.org/10.1016/0304-8853(95)00316-9.

(32) Lefebure, S.; Dubois, E.; Cabuil, V.; Neveu, S.; Massart, R. Monodisperse Magnetic Nanoparticles: Preparation and Dispersion in Water and Oils. *J. Mater. Res.* **1998**, *13* (10), 2975–2981. https://doi.org/10.1557/JMR.1998.0407.

(33) Schneider, C. A.; Rasband, W. S.; Eliceiri, K. W. NIH Image to ImageJ: 25 Years of Image Analysis. *Nat. Methods* **2012**, *9* (7), 671–675. https://doi.org/10.1038/nmeth.2089.

(34) Schindelin, J.; Arganda-Carreras, I.; Frise, E.; Kaynig, V.; Longair, M.; Pietzsch, T.; Preibisch, S.; Rueden, C.; Saalfeld, S.; Schmid, B.; Tinevez, J.-Y.; White, D. J.; Hartenstein, V.; Eliceiri, K.; Tomancak, P.; Cardona, A. Fiji: An Open-Source Platform for Biological-Image Analysis. *Nat. Methods* **2012**, *9* (7), 676–682. https://doi.org/10.1038/nmeth.2019.

(35) Akoglu, H. User's Guide to Correlation Coefficients. *Turk. J. Emerg. Med.* **2018**, *18* (3), 91–93. https://doi.org/10.1016/j.tjem.2018.08.001.

(36) Illien, F.; Rodriguez, N.; Amoura, M.; Joliot, A.; Pallerla, M.; Cribier, S.; Burlina, F.; Sagan, S. Quantitative Fluorescence Spectroscopy and Flow Cytometry Analyses of Cell-Penetrating Peptides Internalization Pathways: Optimization, Pitfalls, Comparison with Mass Spectrometry Quantification. *Sci. Rep.* **2016**, *6* (1), 36938. https://doi.org/10.1038/srep36938.

(37) Swiecicki, J.-M.; Thiebaut, F.; Di Pisa, M.; Gourdin -Bertin, S.; Tailhades, J.; Mansuy, C.; Burlina, F.; Chwetzoff, S.; Trugnan, G.; Chassaing, G.; Lavielle, S. How to Unveil Self-Quenched Fluorophores and Subsequently Map the Subcellular Distribution of Exogenous Peptides. *Sci. Rep.* **2016**, *6* (1), 20237. https://doi.org/10.1038/srep20237.

(38) Iwasaki, T.; Tokuda, Y.; Kotake, A.; Okada, H.; Takeda, S.; Kawano, T.; Nakayama, Y. Cellular Uptake and in Vivo Distribution of Polyhistidine Peptides. *J. Controlled Release* **2015**, *210*, 115–124. https://doi.org/10.1016/j.jconrel.2015.05.268.

(39) Selby, L. I.; Cortez-Jugo, C. M.; Such, G. K.; Johnston, A. P. R. Nanoescapology: Progress toward Understanding the Endosomal Escape of Polymeric Nanoparticles: Endosomal Escape of Polymeric Nanoparticles. *Wiley Interdiscip. Rev. Nanomed. Nanobiotechnol.* **2017**, *9* (5), e1452. https://doi.org/10.1002/wnan.1452.

(40) Chen, J.; Li, J.; Zhou, J.; Lin, Z.; Cavalieri, F.; Czuba-Wojnilowicz, E.; Hu, Y.; Glab, A.; Ju, Y.; Richardson, J. J.; Caruso, F. Metal–Phenolic Coatings as a Platform to Trigger Endosomal Escape of Nanoparticles. *ACS Nano* **2019**, *13* (10), 11653–11664. https://doi.org/10.1021/acsnano.9b05521.

(41) Hu, Y.; Litwin, T.; Nagaraja, A. R.; Kwong, B.; Katz, J.; Watson, N.; Irvine, D. J. Cytosolic Delivery of Membrane-Impermeable Molecules in Dendritic Cells Using PH-Responsive Core−Shell Nanoparticles. *Nano Lett.* **2007**, *7* (10), 3056–3064. https://doi.org/10.1021/nl071542i.

(42) Karnovsky, M. J. 1971. Use of Ferrocyanide-Reduced Osmium Tetroxide in Electron Microscopy. *Abstr. Am. Soc. Cell Biol.* Rockefeller Univ., New York, New Orleans, p.146.

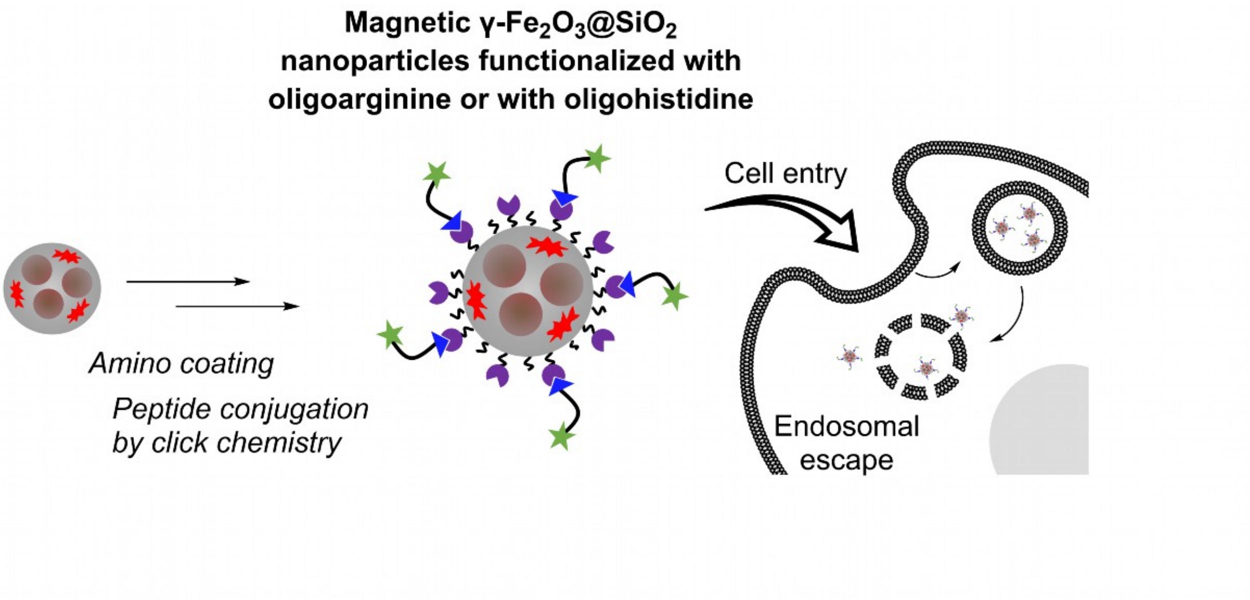
Magnetic γ-Fe2O3@SiO2 nanoparticles functionalized with oligoarginine or with oligohistidine
Amino coating
Peptide conjugation by click chemistry
Cell entry
Endosomal escape